UNIVERSIDAD DE INVESTIGACIÓN DE

TECNOLOGÍA EXPERIMENTAL YACHAY

Escuela de Ciencias Biológicas e Ingeniería

TÍTULO: Finite Element Analysis of vertebral pneumatocyst in arthritic bone alterations with marginal osteophytes and deforming spondylosis in the cervical spine.

Trabajo de integración curricular presentado como requisito para la obtención del título de Ingeniería Biomédica

Autor:

Bernardo Rafael López Falconi

Tutor:

Prof. Fernando Villalba

Urcuquí, enero 2022

Urcuquí, 16 de diciembre de 2021

SECRETARÍA GENERAL
(Vicerrectorado Académico/Cancillería)
ESCUELA DE CIENCIAS BIOLÓGICAS E INGENIERÍA
CARRERA DE BIOMEDICINA
ACTA DE DEFENSA No. UITEY-BIO-2021-00039-AD

A los 16 días del mes de diciembre de 2021, a las 10:00 horas, de manera virtual mediante videoconferencia, y ante el Tribunal Calificador, integrado por los docentes:

Presidente Tribunal de Defensa	Dr. ALMEIDA GALARRAGA, DIEGO ALFONSO , Ph.D.
Miembro No Tutor	Dr. GUDIÑO GOMEZJURADO, MARCO ESTEBAN , Ph.D.
Tutor	MSC VILLALBA MENESES, GANDHI FERNANDO

El(la) señor(ita) estudiante **LOPEZ FALCONI, BERNARDO RAFAEL**, con cédula de identidad No. **0605447259**, de la **ESCUELA DE CIENCIAS BIOLÓGICAS E INGENIERÍA**, de la Carrera de **BIOMEDICINA**, aprobada por el Consejo de Educación Superior (CES), mediante Resolución **RPC-SO-43-No.496-2014**, realiza a través de videoconferencia, la sustentación de su trabajo de titulación denominado: **Finite Element Analysis of vertebral pneumatocyst in arthritic bone alterations with marginal osteophytes and deforming spondylosis in the cervical spine**, previa a la obtención del título de **INGENIERO/A BIOMÉDICO/A**.

El citado trabajo de titulación, fue debidamente aprobado por el(los) docente(s):

Tutor	MSC VILLALBA MENESES, GANDHI FERNANDO

Y recibió las observaciones de los otros miembros del Tribunal Calificador, las mismas que han sido incorporadas por el(la) estudiante.

Previamente cumplidos los requisitos legales y reglamentarios, el trabajo de titulación fue sustentado por el(la) estudiante y examinado por los miembros del Tribunal Calificador. Escuchada la sustentación del trabajo de titulación a través de videoconferencia, que integró la exposición de el(la) estudiante sobre el contenido de la misma y las preguntas formuladas por los miembros del Tribunal, se califica la sustentación del trabajo de titulación con las siguientes calificaciones:

Tipo	Docente	Calificación
Miembro Tribunal De Defensa	Dr. GUDIÑO GOMEZJURADO, MARCO ESTEBAN , Ph.D.	10,0
Tutor	MSC VILLALBA MENESES, GANDHI FERNANDO	10,0
Presidente Tribunal De Defensa	Dr. ALMEIDA GALARRAGA, DIEGO ALFONSO , Ph.D.	10,0

Lo que da un promedio de: **10 (Diez punto Cero)**, sobre 10 (diez), equivalente a: **APROBADO**

Para constancia de lo actuado, firman los miembros del Tribunal Calificador, el/la estudiante y el/la secretario ad-hoc.

Certifico que *en cumplimiento del Decreto Ejecutivo 1017 de 16 de marzo de 2020, la defensa de trabajo de titulación (o examen de grado modalidad teórico práctica) se realizó vía virtual, por lo que las firmas de los miembros del Tribunal de Defensa de Grado, constan en forma digital.*

BERNARDO RAFAEL LOPEZ FALCONI
Firmado digitalmente por BERNARDO RAFAEL LOPEZ FALCONI
Fecha: 2022.01.06 02:39:05 -05'00'

LOPEZ FALCONI, BERNARDO RAFAEL
Estudiante

DIEGO ALFONSO ALMEIDA GALARRAGA
Firmado digitalmente por DIEGO ALFONSO ALMEIDA GALARRAGA
Fecha: 2021.12.20 21:27:23 -05'00'

Dr. ALMEIDA GALARRAGA, DIEGO ALFONSO , Ph.D.
Presidente Tribunal de Defensa

Firmado electrónicamente por:
GANDHI FERNANDO VILLALBA MENESES

MSC VILLALBA MENESES, GANDHI FERNANDO

MARCO ESTEBAN GUDINO GOMEZJURADO

Firmado digitalmente por MARCO ESTEBAN GUDINO GOMEZJURADO
Fecha: 2021.12.16 12:11:45 -05'00'

UNIVERSIDAD YACHAY TECH

Dr. GUDIÑO GOMEZJURADO, MARCO ESTEBAN , Ph.D.
Miembro No Tutor

Firmado electrónicamente por:
KARLA ESTEFANIA ALARCON FELIX

ALARCON FELIX, KARLA ESTEFANIA
Secretario Ad-hoc

AUTORÍA

Yo, **BERNARDO RAFAEL LÓPEZ FALCONI**, con cédula de identidad 0605447259, declaro que las ideas, juicios, valoraciones, interpretaciones, consultas bibliográficas, definiciones y conceptualizaciones expuestas en el presente trabajo; así cómo, los procedimientos y herramientas utilizadas en la investigación, son de absoluta responsabilidad de el/la autora (a) del trabajo de integración curricular. Así mismo, me acojo a los reglamentos internos de la Universidad de Investigación de Tecnología Experimental Yachay.

Urcuquí, enero 2022.

BERNARDO RAFAEL LOPEZ FALCONI

Firmado digitalmente por BERNARDO RAFAEL LOPEZ FALCONI
Fecha: 2022.01.06 02:39:36 -05'00'

Bernardo Rafael López Falconi
CI: 0605447259

AUTORIZACIÓN DE PUBLICACIÓN

Yo, **BERNARDO RAFAEL LÓPEZ FALCONI,** con cédula de identidad 0605447259, cedo a la Universidad de Investigación de Tecnología Experimental Yachay, los derechos de publicación de la presente obra, sin que deba haber un reconocimiento económico por este concepto. Declaro además que el texto del presente trabajo de titulación no podrá ser cedido a ninguna empresa editorial para su publicación u otros fines, sin contar previamente con la autorización escrita de la Universidad.

Asimismo, autorizo a la Universidad que realice la digitalización y publicación de este trabajo de integración curricular en el repositorio virtual, de conformidad a lo dispuesto en el Art. 144 de la Ley Orgánica de Educación Superior

Urcuquí, enero 2022.

BERNARDO RAFAEL LOPEZ FALCONI

Firmado digitalmente por BERNARDO RAFAEL LOPEZ FALCONI
Fecha: 2022.01.06 02:39:53 -05'00'

____

Bernardo Rafael López Falconi
CI: 0605447259

Dedicatoria

Este trabajo le dedico a mi familia; A mi padre quien hizo todo lo que estaba en sus manos para que yo llegara hasta aquí, además de ser la persona que formo mi carácter y educación. A mi madre por ser mi guía que estuvo siempre apoyándome y aconsejándome para ser una mejor persona. A mi hermana que siempre estuvo escuchándome y aconsejándome pese a cualquier cosa.

A mis amigos: Dany, Dilan, Kevincito, Madelein, Majo, Bryan C, Joselyn, Xiomi, Jasmín, Andrés, Gino, Kevin C, Erick, Erika, Kevin P, Mario, Johana, Alanís, Carito, Bryan J, Andy, Robert, Jose Luis.

Bernardo Rafael López Falconi

Agradecimiento

Agradezco infinitamente a la Universidad Yachay Tech por abrirme las puertas, ser mi hogar y ser una fuente de conocimiento para empezar este gran viaje.

Agradezco a mi tutor de tesis Fernando Villalba por acogerme, aconsejarme y motivarme en la realización de este proyecto.

A todos los profesores que formaron parte de mi crecimiento académico y personal. Cada uno de ellos aporto significativamente en mi proceso como profesional.

A mis amigos que estuvieron conmigo en todo momento, y a pesar de cualquier dificultad siempre me tendían una mano. Además de ser mi apoyo incondicional.

Bernardo Rafael López Falconi

Resumen

El método de elementos finitos es utilizado ampliamente para hacer análisis con el fin de ser aplicado en la resolución y diagnóstico de problemas de análisis estructural. El análisis de elementos finitos (FEA) estudia los desplazamientos, deformaciones y tensiones, también permite representar diferentes escenarios y evaluar el rendimiento de productos con aplicación de criterios de resistencia, rigidez o fatiga. En su mayoría los análisis se llevan a cabo mediante uso de softwares que implementan el uso del método de elementos finitos, permitiéndonos obtener respuestas para numerosos problemas de ingeniería, así como también de medicina. El presente estudio consiste en el diseño de un modelo en 3D de las vértebras C5, C6 y C7 a partir del uso de imágenes de tomografía computarizada de un paciente. Las vértebras presentan neumoquistes, espondilosis de formans, osteofitos y disminución de discos intervertebrales. El modelo se generó a través de diferentes programas con el fin de crear un modelo muy similar a las vértebras del paciente. El análisis tiene la finalidad de estudiar el estrés, tensión, desplazamiento (en los ejes de X, Y, y Z) y el factor de seguridad del modelo 3D obtenido.

Palabras Clave:

Cervical, spine, biomechanics, finite elements analysis, pneumatocyst, vertebral pneumatocyst, intervertebral discs, osteoarthritis, 3D model.

Abstract

Es el mismo resumen, pero traducido al idioma inglés. The finite element method is widely used for analysis in order to be applied in solving and diagnosing structural analysis problems. Finite element analysis (FEA) studies displacements, deformations and stresses, it also allows representing different scenarios and evaluating the performance of products with the application of resistance, stiffness or fatigue criteria. Most of the analyzes are carried out through the use of software that implements the use of the finite element method, allowing us to obtain answers for numerous engineering problems, as well as medicine. The present study consists of the design of a 3D model of the C5, C6 and C7 vertebrae from the use of computerized tomography images of a patient. The vertebrae present pneumocysts, formans spondylosis, osteophytes and diminished intervertebral discs. The model was generated through different programs in order to create a model very similar to the vertebrae of the patient. The analysis has the purpose of studying the stress, tension, displacement (in the X, Y, and Z axes) and the safety factor of the 3D model obtained.

Key Words:

Cervical, spine, biomechanics, finite elements analysis, pneumatocyst, vertebral pneumatocyst, intervertebral discs, osteoarthritis, 3D model

Objectives

General

Perform a biomechanical evaluation of the cervical spine of a patient with pneumatocyst.

Specific

- Generate 3D models of the cervical column using Mimics Medical.
- Generate a mesh of the 3D models previously created using Ansys (ICM-CFD).
- Perform the finite element analysis of the generated mesh using Abaqus.

Scope

This research has a qualitative approach since from the application of the FEA it is sought to describe and explore the data obtained, conclude, and later with the information obtained, hypotheses and theories could be generated.

It is cross-sectional since the FEA was applied only once. The research is non-experimental since no variable was manipulated, and it is descriptive since the characteristics resulting from the FEA of vertebrae with pneumatocyst and worn intervertebral discs will be detailed.

Index

Tables List

Figure List

Introduction

The spinal column is made up of 24 vertebrae divided into five sections; cervical, thoracic, lumbar, sacrum, and, coccyx (Gandhi et al., 2019). The vertebral column supports the human in the upright posture; allows movement and locomotion; and it protects the spinal cord and branching spinal nerves (Oliver & Middleditch, 1991; Waxenbaum & Futterman, 2018a; Waxenbaum & Futterman, 2019). In addition, the head houses the sensory apparatus (hearing, sight, smell, and taste). Therefore, the head must have the ability to move to scan the environment. For this, the cervical spine is responsible for the motor skills of the head.

The spinal column can be damaged by different external or internal factors, either due to age, fractures, accidents, as well as diseases such as osteoarthritis, pneumatocysts, osteophytes. These factors affect not only the vertebrae but also the intervertebral discs, endplates, and posterior elements (Adams & Roughley, 2006).

The present study is performed using a mesh generated from Computed Tomography (CT) images of a patient with pneumatocysts, osteoarthritis, and worn intervertebral discs. These patients have symptoms: headaches, severe neck pain, nausea, vomiting, dizziness, and these symptoms are made worse by movement. In addition, they can produce degenerative changes, as well as affect communication with the joint space (Park et al., 2015; Husain et al., 2015). It should be noted that pneumatocysts can contain fluids or air within them. The most common locations for pneumatocysts are the C4, C5, C6, and C7 vertebrae (Husain et al., 2015).

Therefore, to understand this problem, a study was carried out in a 64-year-old male patient with pneumatocyst, which was determined through a descriptive model using the Mimics, ICEM, and, ANSYS. For FEA it is considered a value of 50N of load. To simulate the weight generated by the skull and the affectation that it produces in the affected vertebrae and intervertebral discs.

The purpose of this study is to perform a Finite Element Analysis (FEA) to test the model that will serve to analyze the behavior of intervertebral discs as well as vertebrae with pneumatocysts.

Chapter I: Theoretical Framework

1.1 State of the Art

Gandhi et al., (2019) evaluated a Biomechanical Analysis of the Cervical Spine Following Disc Degeneration, Disc Fusion, and Disc Replacement using Finite Element Analysis (FEA). A 3-dimensional finite element model of the cervical spine (C2-T1) was modified to simulate single-level (C5-C6) and 2-level (C5-C7) degeneration. The results have shown that the discs preserved motion at the implanted level and maintained normal motions at the adjacent nonoperative levels.

Ruberté et al., (2009) evaluated the Influence of single-level lumbar degenerative disc disease on the behavior of the adjacent segments through a FEA study. A FEM of the lumbar spine was previously developed by their research team. The vertebral body cancellous bone, cortical bone, and posterior elements were modeled with a linear isotropic elastic law. The healthy model was modified to simulate a mildly and moderately degenerated disc at the L4–L5 lumbar level. Their results showed that the segmental range of motion during FLEX/EXT bending loads with 800N of follower preload and without preload, fell within one standard deviation of the in-vitro results at all levels except L3–L4 and L4–L5.

Ng et al., (2003) made a Finite Element Analysis of Cervical Spinal Instability Under Physiologic Loading. They use digitized coordinates of a cadaver specimen of a 68-year-old man and finite element mesh generation were merged to construct a detailed finite element model of the lower cervical spine (C4–C6). The results indicate that ligaments play an important role in resisting anterior and posterior shear, flexion, and axial rotation moments. The result also shows that the disc nucleus plays a major role in cervical spine mechanics. Under other physiologic loadings, the disc nucleus is responsible for the initial stiffness of the cervical spine (Ng et al., 2003).

Kumaresan et al., (1998) made a material property sensitivity finite element analysis study of the cervical spine. The cervical spine geometry for the finite element model was obtained from a 33-year-old adult human cadaver free from spinal disease, metastasis, and trauma. The variations in the elastic modulus of the cancellous core, cortical shell, endplates, and posterior elements representing the hard tissues did not affect the external angular motion under all physiologic loading modes. The variations in the modulus of the cancellous core, cortical shell, endplate, and posterior elements (hard tissues) had little effect on the internal stresses of the inferior and superior intervertebral discs.

Doğru (2018) made a nonlinear finite element analysis of the intervertebral disc. Different HU values from .dicom files could be converted to 3D models separately and consequently, the more detailed anatomic model having different biologic structures was generated. The stress increased nearly ten-fold with the severely degenerated model for all moment directions. Though not significant, the stress in the annulus under flexion moment increased more than in the other directions. The results suggest degeneration on the intervertebral discs affects the spine, especially during flexion motion.

Cai et al., (2019) analyses the biomechanical response of the cervical spine under different follower loads. The geometric information of the cervical vertebra (C3-C7) is derived from a CT image of a healthy male subject. The results showed the application of a follower load increased the IDP of each segment in all postures (0N, 50N, 100N, 150N), and the IDP varied nonlinearly with increasing follower load.

Goel & Clausen (1998) made a prediction of load sharing among spinal components of a c5-c6 motion segment using the finite element approach. The anatomic data for the mesh geometry was acquired from a normal, fresh-frozen human cervical spine (CT – T12) of a 68-year-old man. The results have shown that the extension motion of the model was most affected by facet angle changes, whereas flexion was affected the last.

1.2 Theoretical Foundation

1.2.1 Vertebral Column

The vertebral column also knows as the spinal column or spine, forms the central axis of the body's skeleton (Mahadevan, 2018). The vertebral column is conformed of 24 separate bony vertebrae, along with intervertebral discs (Waxenbaum & Futterman, 2018b). That being the case, the vertebral column extends from the skull to the coccyx and it is comprising of five regions: cervical, thoracic, lumbar, sacral, and coccygeal. Subsequently, from above downwards these comprise seven cervical vertebrae (From C1 to C7); twelve thoracic vertebrae (from T1 to T12); five lumbar vertebrae (from L1 to L5); the sacrum (S3 to the lower sacrum); and coccyx (Bakkum, 2013). The cervical, thoracic and lumbar vertebrae are called "moveable vertebrae", as a result of the fact that the individual vertebrae can move relative to their neighboring vertebrae (Mahadevan, 2018). On the other hand, the sacrum and coccyx are termed immoveable for opposite reasons. The sacrum and coccyx, are each formed by the fusion of five vertebrae to form the sacrum while four fused vertebrae form the coccyx (Mahadevan, 2018; Oliver & Middleditch, 1991). Furthermore, the spine has four physiological curvatures; Cervical lordosis: posterior concavity curvature; Thoracic kyphosis: anterior concavity curvature; Lumbar lordosis: posterior concavity curvature; Sacral kyphosis: anterior concavity curvature (Juan et al., 2018). Finally, the vertebral column contains the spinal cord within the vertebral canal and thereby protects the spinal cord from external trauma. (Mahadevan, 2018).

1.2.2 The function of the Vertebral Column

The vertebral column has three principal functions: It supports the human in the upright posture (support for thorax and abdomen); It allows movement and locomotion; and finally, it protects the spinal cord and branching spinal nerves (Oliver & Middleditch, 1991; Waxenbaum & Futterman, 2018b; Waxenbaum & Futterman, 2019). Thus, when the vertebral column is viewed from the sagittal plane, the vertebral column displays five curves in the upright posture; two cervical, and one thoracic, one lumbar, and one sacral. Nevertheless, the shape of these curves varies in normal spines, and it is frequently altered by pathological changes (Oliver & Middleditch, 1991). The main function of the spinal curves is to help to dissipate vertical compressive forces, thereby, these curves provide a shock-absorbing capacity to the spine (Oliver & Middleditch, 1991). If the case that the vertebral column was straight, vertical compressive forces would be transferred through the vertebral bodies to the intervertebral discs alone. (Oliver & Middleditch, 1991).

On the cervical column, there are two normally-occurring curves: the upper cervical curve extending from the occiput to the axis, and the longer lordotic curve of the lower cervical spine extending from the axis to the second thoracic vertebra. The lower cervical curve is convex forwards and is the reverse of the upper cervical curve. The thoracic curve is extending from T2 to T12 and it is concave forwards and it is because of the greater depth of the posterior parts of the vertebral bodies. Additionally, the lumbar curve is convex forwards and extends from T12 to the lumbosacral junction. Finally, the sacral curve extends from the lumbosacral junction to the coccyx (Oliver & Middleditch, 1991).

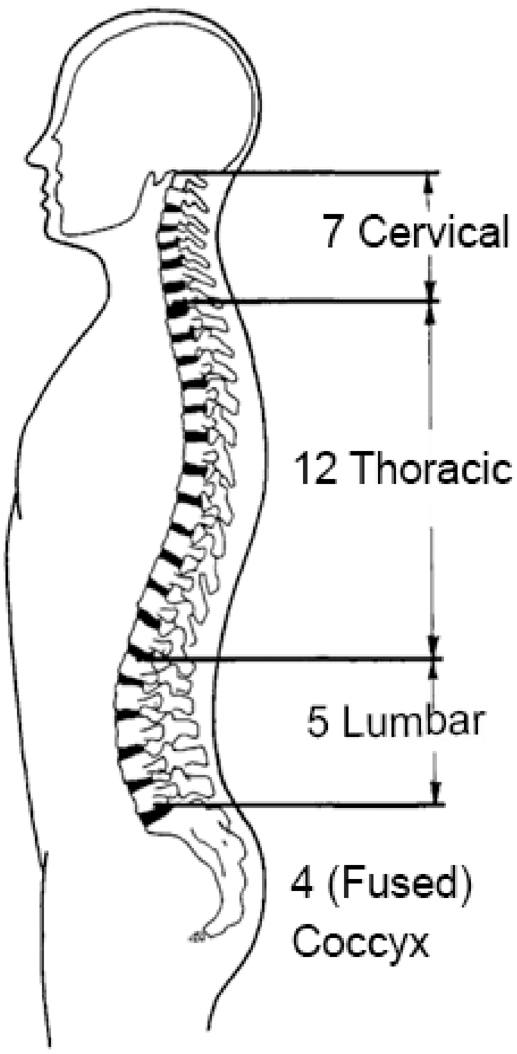

Figure 1: Curvatures of the cervical spine. Own elaboration from Oliver & Middleditch (1991).

1.2.3 Morphology of a vertebra

All the moveable vertebrae, whether from the cervical, thoracic or lumbar regions, share a common morphological design. Thereby, each typical moveable vertebra features a cylindroid vertebral body, anteriorly. At the back of the body is affixed a bony arch, commonly termed the vertebral arch or neural arch. Then, in the center of the vertebrae is called the vertebral foramen (Mahadevan, 2018; Oliver & Middleditch, 1991).

Projecting laterally from the vertebral arch on either side is the corresponding transverse process. Alternatively, projecting backward from the posterior midline of the vertebral arch is the spinous process. The part of the vertebral arch that lies between the roots of the transverse and spinous processes is termed the lamina, on account of its thick and plate-like shape (Mahadevan, 2018).

The superior surface of a vertebra is concave transversely and convex anteroposteriorly and on each side are prominent elevations which are known as the uncinate or unciform processes (Oliver & Middleditch, 1991). Furthermore, the inferior surface is reciprocally convex transversely, and the anteroposteriorly is concave. There are two articular facets on the inferior surface that articulates with the uncinate processes of the subjacent vertebra, known as the joints of Luschka or the uncovertebral joints (Oliver & Middleditch, 1991). The anterior surface of the vertebral body is convex transversely. Them, at the superior and inferior margins it is marked by the fibers of the anterior longitudinal ligament. Finally, the posterior surface of the body is flattened and has foramina for two or more basivertebral veins (Oliver & Middleditch, 1991).

In an articulated vertebral column, all the vertebral foramina are “stacked” one on top of the other, together composing the vertebral canal or also known as the spinal canal. Within the spinal canal is the spinal cord. The spinal cord is occupying the upper two-thirds of the length of the vertebral canal, which in the adult ends at the level of the first lumbar vertebra (Mahadevan, 2018).

The right and left laminae meet in the posterior midline at the root of the spinous process. Also, the most anterior part of the vertebral arch on each side, where the arch adjoins the back of the vertebral body, is termed the pedicle. The height of each pedicle is approximately half the height of the vertebral body. Thus, there is a substantial gap between successive pedicles (intervertebral foramen) (Mahadevan, 2018).

Each intervertebral foramen transmits a spinal nerve with accompanying radicular arteries and veins. Projecting upwards from the vertebral arch on either side of the midline, at approximately the junction of the lamina, pedicle, and the root of the transverse process, is the superior articular process, process while projecting inferiorly from the vertebral arch in line with the superior articular process is the inferior articular process. Each articular process features a smooth articular facet that in life, is covered by a layer of articular hyaline cartilage (Mahadevan, 2018).

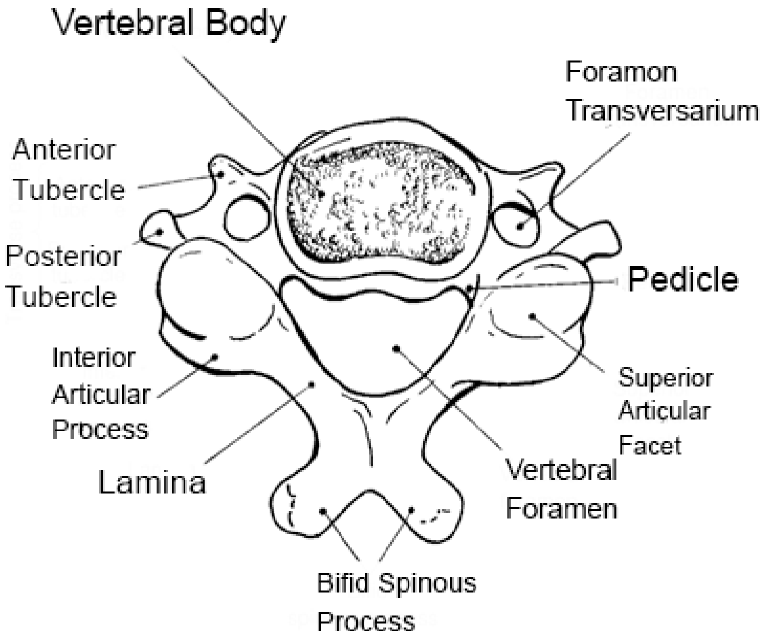

Figure 2: A typical cervical vertebra – superior aspect. Own elaboration from Oliver & Middleditch (1991).

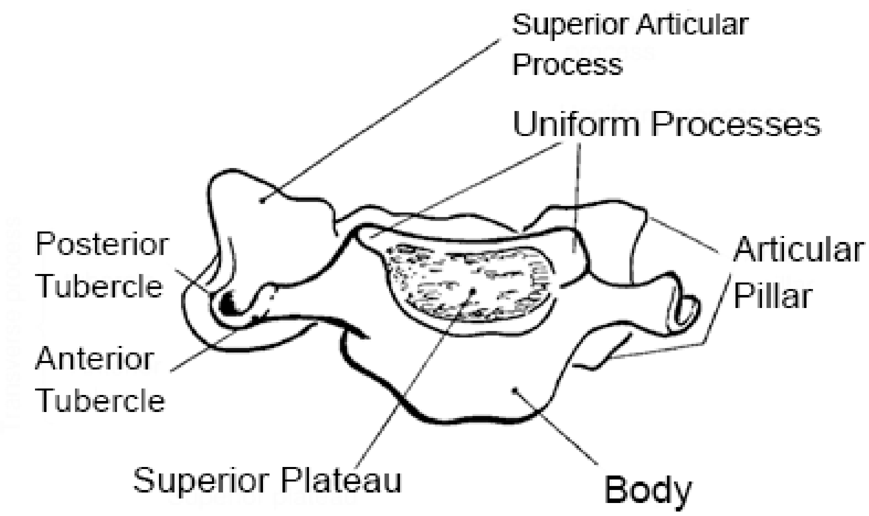

Figure 3: A typical cervical vertebra – anterior aspect. Own elaboration from Oliver & Middleditch (1991).

1.2.4 Intervertebral disks

Intervertebral discs have the function of resisting spinal compression while permitting limited movements and also are spread loading evenly on the nearby vertebrae. The intervertebral discs are in charge of the mobility without sacrificing the supportive strength of the vertebral column (Waxenbaum & Futterman, 2018b). Intervertebral discs are like pads but of fibrocartilage (Adams & Roughley, 2006). The anatomy of an intervertebral disk is composed of; the individual lamellae of the annulus consisting primarily of collagen type I fibers passing at an angle between vertebrae; and, the nucleus pulposus consisting of a proteoglycan and water gel held together loosely by an irregular network of fine collagen type II and elastin fibers (Adams & Roughley, 2006).

Intervertebral discs are generally named according to the vertebra found immediately above the disc. Therefore, if the disc is located between the T6 and T7 vertebrae it carries the T6 as a name. Intervertebral discs are located between the anterior portions of the movable vertebrae and between L5 and the sacrum. Except for the first (C1, atlas) and second (C1 - C2, axis) cervical vertebrae, there is an intervertebral disc between (Oliver & Middleditch, 1991; Bakkum, 2013). Subsequently, by pulling a miniature pressure transducer through, it is possible to study the internal mechanical functioning of an intervertebral disc. Notably, a young healthy disc has a behave similar to a water bed, with the high water content of the nucleus and inner annulus enabling the tissue to act as a fluid (Adams & Roughley, 2006).

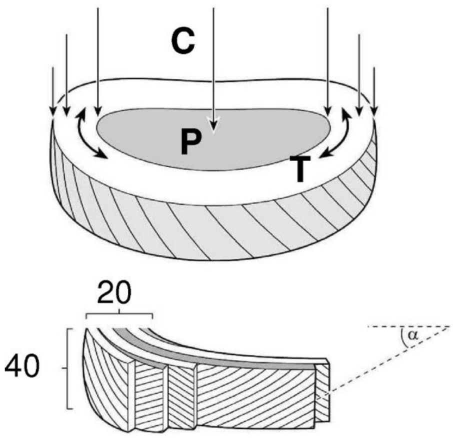

Figure 4. Intervertebral disc structure and function. Upper, spinal compression (C) generates a hydrostatic pressure (P) in the nucleus and tensile stresses (T) in the annulus. Lower, Lamellae of the annulus with oblique collagen fibers in alternating directions (approximately, $\alpha = 30°$) (Adams & Roughley, 2006).

1.2.5 Structure and function of the Cervical Spine

The cervical spine can be divided into three zones that differ in structure and function: the suboccipital zone (centered on the C1 vertebra); a transitional zone (formed by the C2 vertebra); and the typical zone, (encompassing the C–7 vertebrae) (Bogduk, 2016; Bakkum, 2013). Cervical vertebrae have distinct features from those of the thoracic or lumbar vertebrae. The most notable distinction is the presence of one foramen, in each transverse process in charge of encircling the vertebral arteries and veins (Waxenbaum & Futterman, 2018a). Nevertheless, the C7 vertebrae's foramina contain only accessory veins (Waxenbaum & Futterman, 2018a).

The smaller size of cervical vertebrae relative to the other regions is a reflection of their decreased load-bearing requirements. Their decreased size allows for the greatest range of motion of all vertebral segments (Waxenbaum & Futterman, 2018a). The transverse and spinous processes serve as points of attachment and leverage for cervical and upper thoracic musculature. C1 vertebrae (Atlas) have the lowest load-bearing requirement of all vertebrae, which accounts for their small size and lack of vertebral body (Waxenbaum & Futterman, 2018a).

The positioning of the lateral masses and the absence of the body allows for the majority of the motion in the sagittal plane (cervical flexion and extension) to occur through the atlantooccipital joint (Waxenbaum & Futterman, 2018a). The dens of C2 serve as an axis around which C1 rotates. Furthermore, allowing the rotation of the head in the transverse plane. In fact, due to the size of the intervertebral discs and the orientation of the facet joints, the cervical region has the greatest flexion ability of the spinal column (Waxenbaum & Futterman, 2018a).

1.2.6 Biomechanical Characteristics of the Cervical spine and Functional anatomy of the Cervical Spine

In the human head, the muscles are in charge of the movement of the head but the type of movements possible entirely depends on the shape and structure of the cervical vertebrae and interplay between them (Bogduk & Mercer, 2000). Therefore, the kinematics of the cervical spine are predicated by the anatomy of the bones that make up the neck and the joints that they form. Kinematics can study the normal range of motion (ROM) of each segment in the 3D space, without the influence of other internal or external forces (Menchetti, 2015). As a rule, the range is expressed by translation and rotation in three planes. It is considered that too much motion on the spine can cause structural damage, on the contrary, too little motion may accompany stiffness and pain (Menchetti, 2015).

Additionally, the motion segment is the "Functional Spine Unit" or FSU that consists of two adjacent vertebrae and the interconnecting soft tissue. Forces applied to the spine can always be separated into component vectors. If a force vector acts on a lever, known as “moment arm”, a bending moment is generated. This bending moment applied to a point in the space causes rotation about an axis: this axis is defined “instantaneous axis of rotation” or IAR (Menchetti, 2015). Moreover, using the standard Cartesian coordinate system (x, y, z) for the spine, It can be considered 12 potential movements about the IAR (2 translational and 2 rotational along or around each axes) (Menchetti, 2015). On the cervical movement, when a cervical segment moves, there are 6° of freedom that exists about each IAR. When an FSU is loaded, the motion behavior is affected by the choice of the point at which the load or torque is applied (Menchetti, 2015).

The balance point is achieved when an axial load creates nearly pure compression and the out of a plane is minimized (Menchetti, 2015). Any loading out of this point causes a moment and induces bending. The rotation occurs if the couple is unopposed. As stressed, the couple is different from “coupling”. This term indicates the phenomenon whereby a movement of the spine obligates a separate motion about another axis. In the lower cervical spine is typical that the lateral bending results in axial rotation of the spinous processes away from the concave side of the direction of the bend (Menchetti, 2015).

At the C2 through C3 junction, the body of the axis acts like a root within C3, which means that it is securing the upper cervical spine in the remaining cervical column (Bogduk & Mercer, 2000). Furthermore, the articulating surfaces of the inferior and superior intervertebral joints are like a saddle joint, in other words, they are maintaining anterior/posterior and, medially/laterally directed concavities (Penning & Wilmink, 1987). The global physiological ROM in the cervical spine is approximately 90° of flexion, 70° of extension, 20° to 45° of lateral bending, and up to 90° of rotation on each side (Tan et al., 2017).

The cervical spine can be divided into 5 units, each with unique morphology that determines its kinematics. The units are the occipito-cervical junction (C0–C1); the atlas (C1); the axis (C2); C2–C3 junction; C3–C7 levels (Menchetti, 2015). Through high-speed cineradiography, it was determined that flexion is initiated at the lower cervical spine (C4 through C7), followed by motion at C0 (occiput) through C2, C2 through C3, and then C3 through C4 (Swartz et al., 2005). The C6 through C7 segment undergoes a brief reversal of motion into extension, followed by a reversal of motion at C0 through C2. The C6 through C7 segment contributes to the end ranges of flexion (Swartz et al., 2005). The extension is also initiated in the lower cervical spine (C4 through C7) and is followed by the beginning of motion at C0 through C2 (Swartz et al., 2005). The middle range consists of a varied movement from the mid-cervical region, whereas the lower cervical spine is the last to contribute as the column moves into terminal extension (Swartz et al., 2005).

1.2.7 Pathologies of the Patient

1.2.7.1 Pneumatocyst

A Pneumatocyst a benign, usually asymptomatic, gas-filled lesion found in bone especially of the ilium, sacrum, or spinal vertebra. The term “intraosseous pneumatocyst” was first used by Ramirez et al. for a gas-containing bone cyst adjacent to the sacroiliac joint difficult to detect because of the inherent density of bone (Ramirez et al., 1984). These lesions are asymptomatic and are detected incidentally during imaging examinations. Although gas collection in degenerated intervertebral disks (vacuum phenomenon) is common, however intraosseous gas collection is much less common (Nakayama et al., 2001; Husain et al., 2015). The gas collection is reported in pathologic proses such as osteomyelitis, collapsed vertebral bodies (Kummell disease), penetrating trauma, postsurgical change, and also observed in a simple bone cyst (Nakayama et al., 2001).

A Pneumatocyst is normally present only in the craniofacial bones in human beings. Intraosseous air at other locations is infrequently noted in conditions like osteomyelitis, irradiated neoplasms, intraosseous ganglia, osteonecrosis, methyl methacrylate prosthesis, and postoperative and posttraumatic states (Sen et al., 2015). This is a relatively unknown cystic lesion that frequently affects the sacroiliac joint but is also observed within the cervical vertebrae. It is stated that the sizes of pneumatocysts remain stable based on radiological examinations (Park et al., 2015). Manifestation in the cervical spine has been reported as uncommon but currently is described as more common than previously believed (Husain et al., 2015).

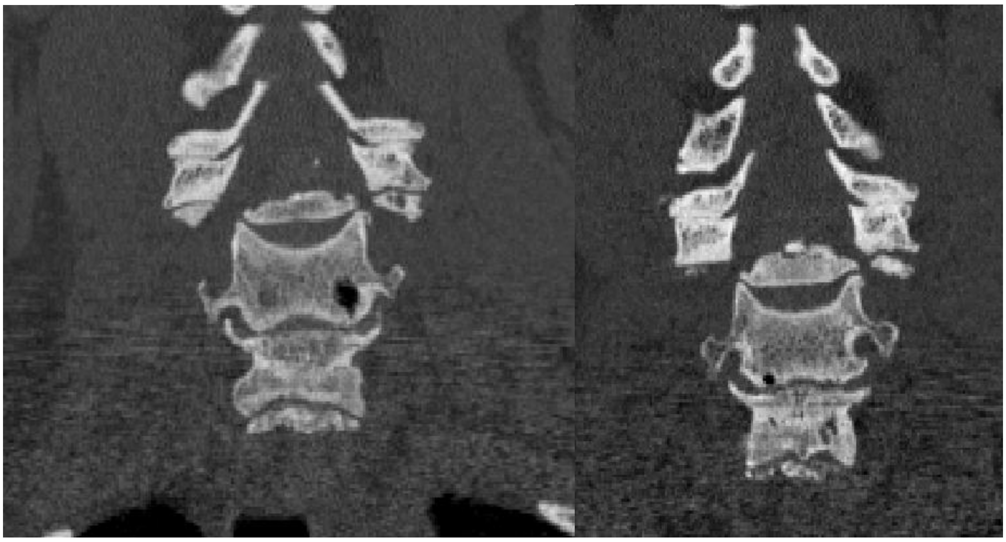

Figure 5: Coronal view of the pneumatocyst (Taken from the CT of the patient)

Figure 6: Axial view of the pneumatocyst (Taken from the CT of the patient)

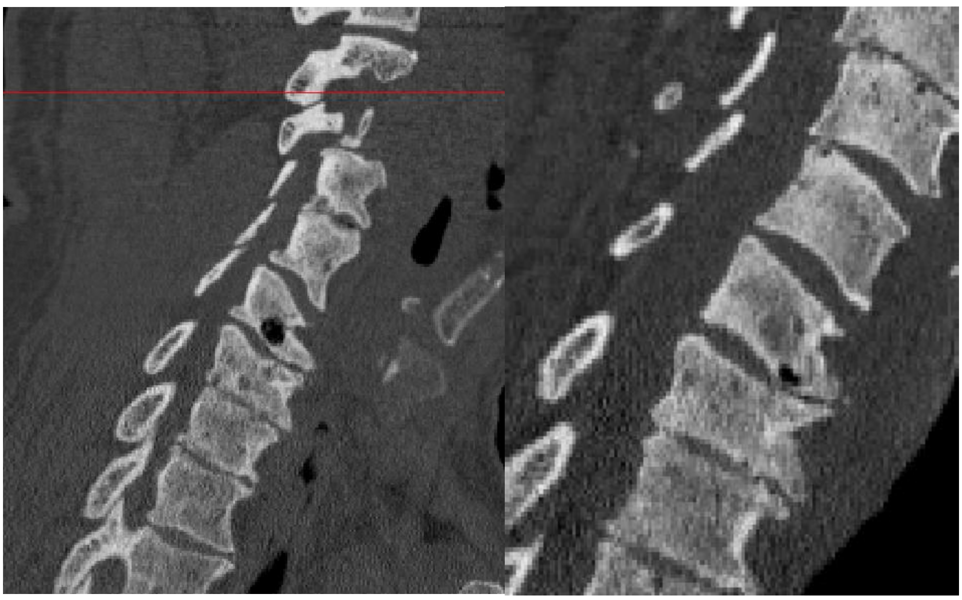

Figure 7: Sagittal view of the pneumatocyst (Taken from the CT of the patient)

Treatments for Pneumatocyst

Treatment is typically not required for the intravertebral pneumatocyst. Sometimes, the lesions become large enough to occupy most of the vertebral body, in which case the possibility of vertebral fracture may be a concern. In such cases, surgical intervention has been proposed. At present, however, there are no documented cases of vertebral surgery to treat a pneumatocyst or a pathologic fracture at the site of a preexisting lesion (Husain et al., 2015). Although percutaneous injection of bone graft substitute material for the treatment of a symptomatic pneumatocyst was reported as a treatment option, they are nearly always treated conservatively (Park et al., 2015).

1.2.7.2 Osteoarthritis (osteoarthrosis or degenerative joint disease)

Osteoarthritis is a "heterogeneous group of conditions that lead to joint symptoms and signs, which are associated with defective integrity of articular cartilage, in addition to related changes in the underlying bone at the joint margins (Altman et al., 1986).

The disorder occurs due to altered local mechanical factors including joint malalignment, muscle weakness, injury, previous knee surgery, occupational bending, and lifting, or meniscal tears (Weissman, 2009).

Figure 8: Degenerative Joints (Intervertebral Discs) (Taken from the CT of the patient). Note: Red squares enclose sections where intervertebral discs are worn.

1.2.7.3 Osteophyte

An osteophyte is a fibrocartilage-capped bony outgrowth (van der Kraan & van den Berg, 2007). Furthermore, osteoarthritis is a disease of hyaline articular cartilage, the disorder is now believed to involve the entire joint including cartilage, bone, ligaments, menisci, periarticular muscles, capsule, and synovium (Weissman, 2009). In fact, osteophytes can form early in the development of osteoarthritis and can be seen before joint space narrowing (van der Kraan & van den Berg, 2007).

Figure 9: Osteophytes of the CT images (Taken from the CT of the patient).

Notes: The red arrows point to the bumps that form on the vertebrae.

1.2.7.4 Spondylosis Deformans

Spondylosis deformans are osteophytosis of the endplates. It is thought to be secondary to anterolateral disc displacement, which results in traction at the site of osseous attachment of the annulus (Thomas & Fingeroth, 2015).

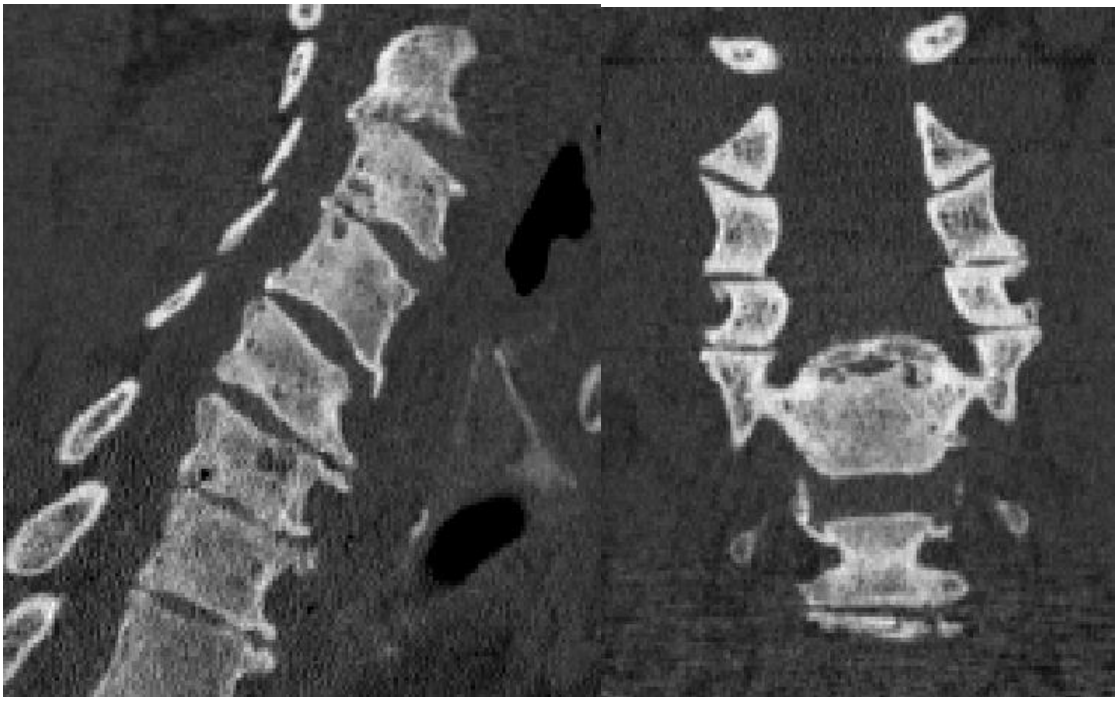

Figure 10: Overall deformation of intervertebral discs and vertebrae (Taken from the CT of the patient)

Figure 11: Overall deformation of intervertebral discs and vertebrae (Taken from the CT of the patient)

1.2.8 Finite element analysis (FEA)

The concept of geometrical division can be seen from the Archimedes time, who for computing the area of an unusual shape, divided the whole shape into equal triangles and quadrilaterals whose areas can be easily worked out and the addition of all areas is the total area of the unusual shape (Zienkiewicz, 2013; Bibhuti Bhusan-Das, Salim Barbhuiya, Rishi Gupta, 2019). Bone is the most frequently investigated biological material and finite element analysis (FEA) is currently the computational tool most commonly used for the analysis of bone biomechanical function and has had a substantial impact on our understanding of the complex behavior of bone (Ruffoni & Van Lenthe, 2017).

1.2.8.1 Finite element analysis Method

The finite element method (FEM) is a numerical technique used to obtain an approximate solution for the problems involving elliptical partial differential equations with boundary conditions by dividing the whole domain into several finite elements as per the problem (Bibhuti Bhusan-Das, Salim Barbhuiya, Rishi Gupta, 2019). Therefore mathematics is the necessary technique to understand any problem comprehensively and quantify stresses, strains, displacements of any physical phenomena of a structure and these are described by using partial differential equations (Bibhuti Bhusan-Das, Salim Barbhuiya, Rishi Gupta, 2019).

Since 1960, were developed computer programs for FEA, incorporating computer graphics which made FEA more attractive to be used for design purposes. NASTRAN, ANSYS, and FEAST are software that can be written in any computer language like C, C++, facilitating any type of engineering problem in less time. This technique is adopted by engineers to decrease the number of physical examples, experiments and modify the components in the design procedure for better products in a quicker way (Bibhuti Bhusan-Das, Salim Barbhuiya, Rishi Gupta, 2019).

In FEA, two typical drawbacks are resulting from the element discretization should be mentioned (Ruffoni & Van Lenthe, 2017). First, the displacement functions can very well represent the displacement field within each element but may give rise to a discontinuity in the displacement between adjacent elements, therefore violating the compatibility criterion (Ruffoni & Van Lenthe, 2017). Second, equilibrium is computed and ensured only at nodes where equivalent forces are considered; inside the element's equilibrium requirements are often violated (Ruffoni & Van Lenthe, 2017). As a consequence, the solution obtained with FEA is approximate and concepts like accuracy and validity should be considered (Ruffoni & Van Lenthe, 2017).

Nevertheless, the accuracy of a FE model quantifies how close the model output is to the real solution of the boundary-value problem (Ruffoni & Van Lenthe, 2017). Since the real solution is not known, the accuracy can be estimated with a so-called convergence test: the size of the element is decreased and a new solution is obtained and compared with the old one (Ruffoni & Van Lenthe, 2017). The validation of a model is often performed by comparing model predictions with experimental results (Ruffoni & Van Lenthe, 2017).

1.2.8.2 Basic Procedure and Applications of FEM

The application of FEM has been implemented into static structural problems, steady-state thermal, hydrodynamic problems, magnetostatic analysis, eigenvalues problems, fluid flow problems, etc (Zienkiewicz, 2013). In solving any type of problem, few basic steps are followed in every analysis of FEM. Finite element analysis can use more than one material within a single structure such as isotropic, orthotropic, and anisotropic. Al the equations were taken from: Bibhuti Bhusan-Das, Salim Barbhuiya, Rishi Gupta, 2019; Levyakov, (2011).

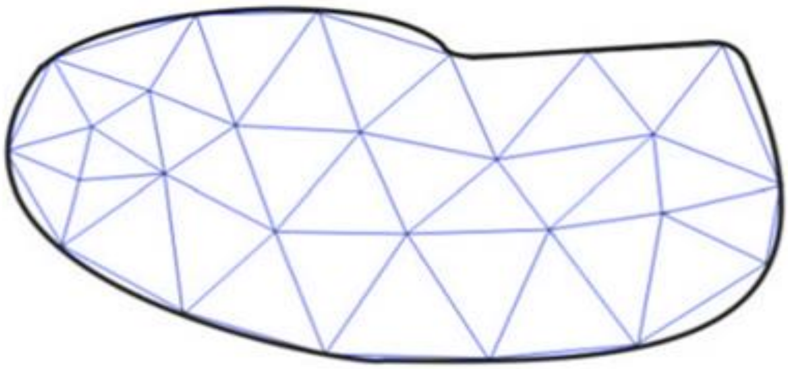

Figure 12: Triangular Elements. Own elaboration from Bibhuti Bhusan-Das et al (*2019).*

The equilibrium equations for various cases are:

1. Linear static:

$$Ku = F \tag{1}$$

2. Linear dynamic:

$$Mu^{'}(t) + Cu^{'}(t) + Ku(t) = F(t) \tag{2}$$

3. Non-linear static:

$$Ku + F_{NL} = F \tag{3}$$

4. Non-linear dynamics:

$$Mu^{'}(t) + Cu^{'}(t) + Ku(t) + F_{NL}(t) = F(t) \tag{4}$$

Where the variables are explained on table 1.

Table 1: Legend of FEA equations

M	Mass of the structure
C	Damping of the structure
K	Stiffness of the structure
F	Force of the structure
U	Displacement of the structure

Note: Legend of the variables of the equations.

In general, the FEM we use today for analysis involves steps of:

1. Discretization of the whole continuum into subdivisions known as finite elements and these elements are interconnected by the nodes.
2. Discretization of the whole continuum into subdivisions known as finite elements and these elements are interconnected by the nodes.
3. At first, the element type is chosen like beam element, plate element, shell element, solid element and according to it the degree of freedom is considered at each node.
4. Identifying the variables (displacements, stress, temperature, pressure, etc.) on the nodal points.
5. As we do not know the variation of the variable field inside the whole body, it is assumed that this variation is approximated by using a function known as approximating function (Φ).

$$\{u\} = 1 + x + y + x^2 + xy + y^2 \tag{5}$$

A displacement function is chosen that shows the displacement variation inside the element and then it is approximated in form of a linear function.

$$u = N_1\mu_1 + N_2u_2 + \cdots \tag{6}$$

$$v = N_1v_1 + N_2v_2 + \cdots \tag{7}$$

6. Formation of the elemental and global stiffness matrix for the elements by considering the number and the degree of freedom of the nodal points.
   The total number of degrees of freedom = number of nodes × DOF of one node
   The size of the elemental stiffness matrix = total number of DOF, which is always a square matrix. Then the global stiffness matrix is formed by combining all the small elemental stiffness matrices.

$$k_e = t_eA_eB^TDB \tag{8}$$

7. Formation of the elemental and global load matrix for the elements by considering the problem.

$$\{F_e\} = \begin{bmatrix} F1 \\ F2 \\ F3 \end{bmatrix} \tag{9}$$

   Then the global load matrix is formed by assembling the elemental load matrices.

8. Then by incorporating the boundary conditions into the problem the stiffness matrix is reduced and by applying the simultaneous equation finally the variables and stress resultants are calculated.

$$[k] = \{\delta\}\, x\, \{F\} \tag{10}$$

   The stress in the member is calculated by,

$$\{\sigma\} = [D]\, x\, [B]\, x\, [\delta] \tag{11}$$

   The reactions at the supports are calculated as,

$$\{R\} = [K]\, x\, \{\delta\} - \{F\} \tag{12}$$

Chapter II: Materials and Methods

2.1 Tools & Software Used

2.1.1 RadiAnt DICOM Viewer

Is an application for processing and displaying medical images in DICOM format (Digital Imaging and Communications in Medicine). Studies obtained from different imaging modalities can be displayed in RadiAnt DICOM Viewer: Digital Radiography (CR, DX); Mammography (MG); Computed Tomography (CT); Magnetic Resonance (MR); Positron Emission Tomography PET-CT (PT); Ultrasonography (US, IVUS); Digital Angiography (XA); Gamma camera, Nuclear medicine (NM); Secondary Pictures and Scanned Images (SC); Endoscopy (ES); Microscopy (SM, GM); Structured Reports (SR); Encapsulated PDF Documents (OT).

The viewer can handle many types of DICOM images: Monochromatic (CR, CT, MR) and color; Static images (CR, MG, CT) and dynamic sequences; Uncompressed and compressed (RLE, JPEG Lossy, JPEG Lossless, JPEG 2000, JPEG-LS) (*Welcome to RadiAnt DICOM Viewer*, n.d.).

2.1.2 Mimics Medical

Mimics Medical is intended for use as a software interface and image segmentation system for the transfer of medical imaging information to an output file. Mimics Medical is also intended for measuring and treatment planning. The Mimics Medical output can be used for the fabrication of physical replicas of the output file using traditional or additive manufacturing methods. The physical replica can be used for diagnostic purposes in the field of orthopedic, maxillofacial, and cardiovascular applications (García Reyes, 2013).

2.1.3 ANSYS ICEM CFD

ICEM is a software developed by ICEM CFD engineering which provides sophisticated geometry tools for CAO, mesh generation, post-processing, and mesh optimization tools. It is used for engineering applications such as computational fluid dynamics and structural analysis. ICEM CFD also offers tools for post-processing and mesh optimization (*A Quick Overview of ICEM*, n.d.).

2.1.4 Abaqus

ABAQUS is a general-purpose finite element analysis CAE software as part of Dassault Systemes' SIMULIA platform. SIMULIA provides a portfolio of 3D finite element analysis and simulation solutions, including CATIA Analysis applications, Abaqus for unified finite element analysis, multiphysics solutions, and solutions for simulation, process, and intellectual property information lifecycle management. SIMULIA makes realistic simulations an integral business practice that improves product performance, reduces the use of physical prototypes, and drives innovation. It extends the functionality of CATIA Analysis and Abaqus products by allowing the user to perform thermal and nonlinear analysis directly on their CATIA geometry, taking advantage of the robust Abaqus FEA technology (*ABAQUS Software de Analisis y Simulacion CAE*, n.d.).

2.2 Methodology

Through the present investigation, we can know the behavior of the intervertebral discs of a patient with osteoarthritis, worn intervertebral discs, and pneumatocysts, through finite elements.

For the development of meshing for finite element analysis carried out in Abaqus, different steps were followed through the use of different programs. The development of the FEA was carried out on a computer using different computational resources, as well as useful programs that were used to process the CT images. The final mesh was developed on a desktop with an Intel (R) Core (TM) i7-4470 processor with a CPU @ 3.40GHz, with 16 Gb of RAM. The tools and methods used will be explained below.

The following flow chart (Figure 13) is made in order to understand the different required steps in order to accomplish the FEA.

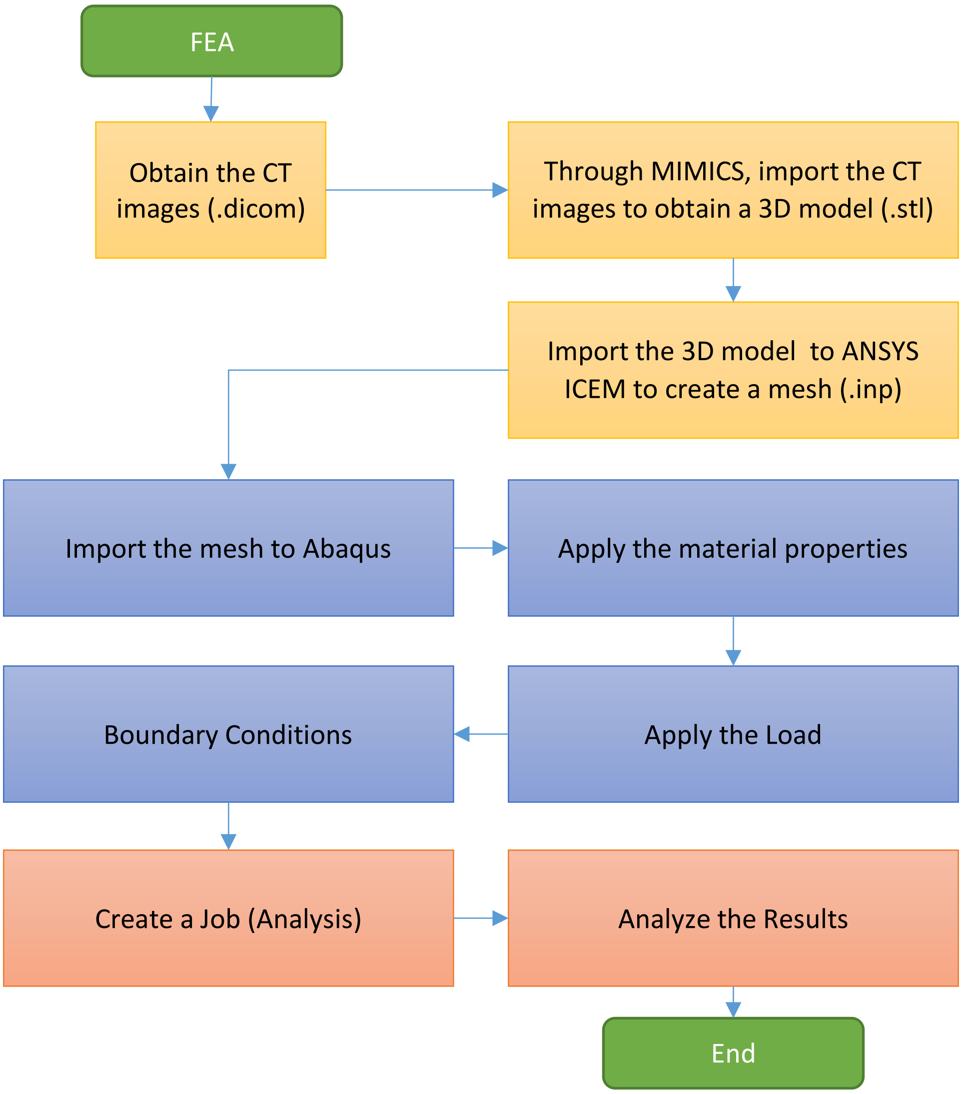

Figure 13: Flow chart of the FEA.

2.3 Data/Model acquisition and information processing

2.3.1 Tomography of the cervical spine

The tomographic study of the cervical spine with cross-sectional tomographic sections and two-dimensional and three-dimensional multi-planar reconstructions on a 64-year-old male patient (*BIMCV*, n.d.).

The CT scans showed:

– Normal cranio-odontoid and/or cranio-cervical junction with calcifications of the alar and/or paraodontoids ligaments.

– Evident osteoarthritic and/or degenerative bone alterations with marginal osteophytes and spondylosis deformans.

– Asymmetry and decrease in the width of the intervertebral spaces between C3-C4, C4-C5, C5-C6, C6-C7 with possible disc-radiculopathies at this level.
– Rectification of physiological lordosis.
– Vertebral canal with preserved anterior-posterior diameters.
– Arthrosic signs of the vertebral bone structures of the posterior cervical wall with asymmetry of the intervertebral spaces.

2.3.2 Visualization of tomographic images

The Radiant Dicom Viewer program was used for the visualization of the tomographic images. Mimics Medical fulfills the same visualization function as Radiant Dicom Viewer but adds the function of being able to create a 3D model based on the tomographic images obtained.

Figure 14: Dicom Viewer Interface 1

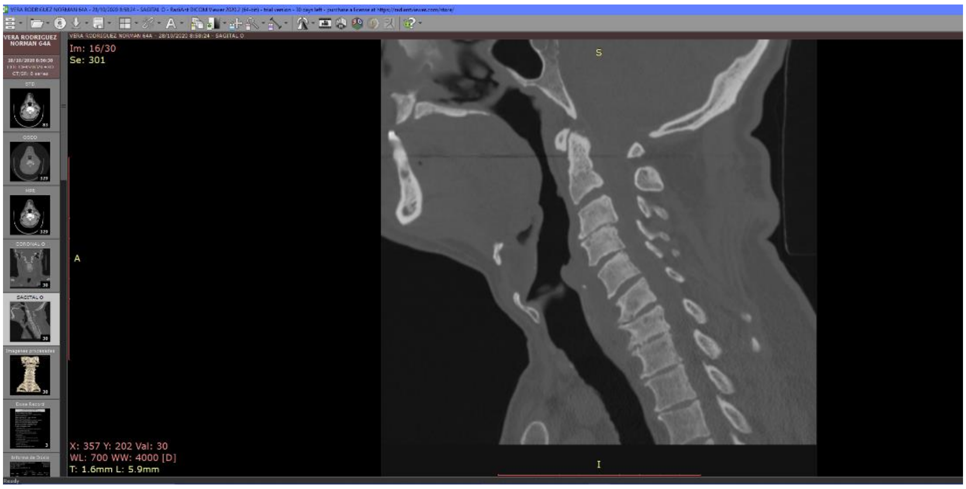

Figure 15: Dicom Viewer Interface 2

The images (.dicom) were imported into the Mimics Medical program. Once the images were imported, they were edited one by one to generate a 3D model as accurately as possible. For this study, a model of three vertebrae (C5 C6 C7) was generated.

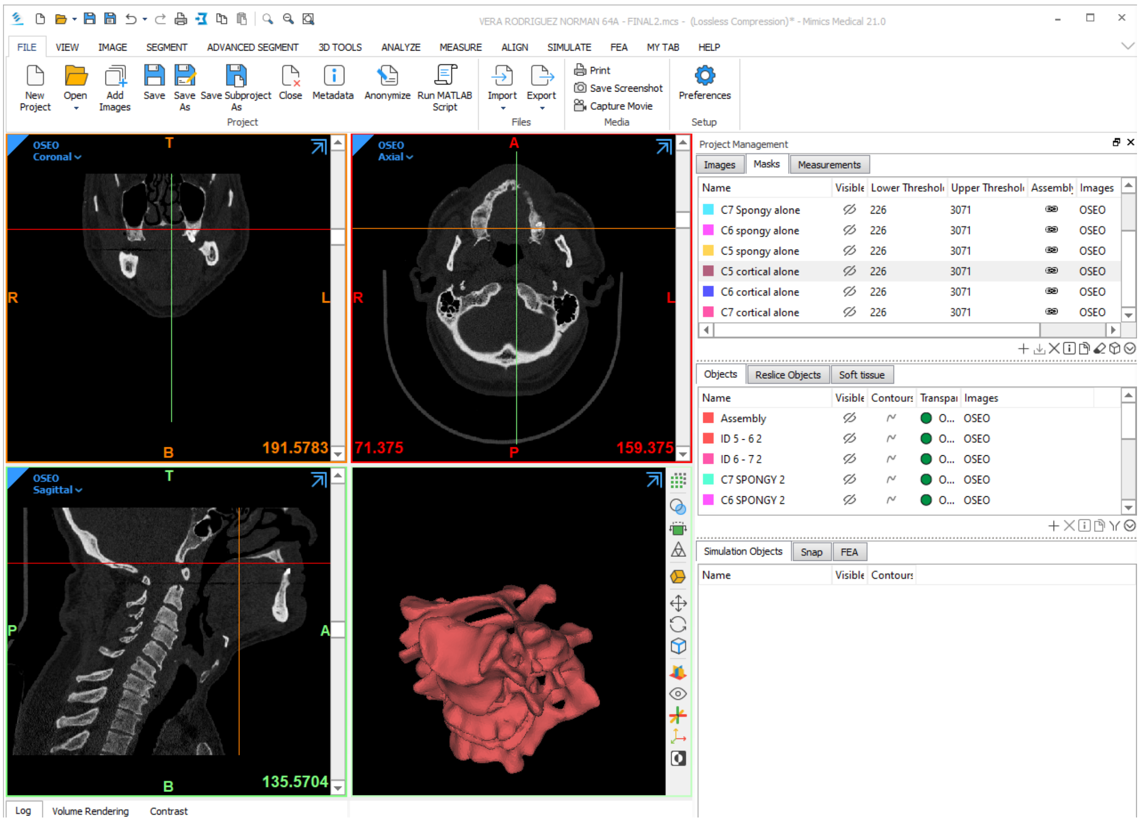

Figure 16: Mimics Interface.

The CT images were painted in such a way as to obtain a section of cortical bone and a section of cancellous bone for each vertebra, as well as a section of each intervertebral disc. However, models of the endplates were not used because the patient's intervertebral discs were destroyed due to osteoarthritis. It should be emphasized that morphological changes to the endplates are usually seen with advancing age but are also evident in association with pathological changes to the nucleus and annulus in advanced stages of degenerative disc disease (Moore, 2006). The endplates are typically less than 1 mm thick, and while this varies considerably across the width of any single disc, they tend to be thinnest in the central region adjacent to the nucleus (Moore, 2006).

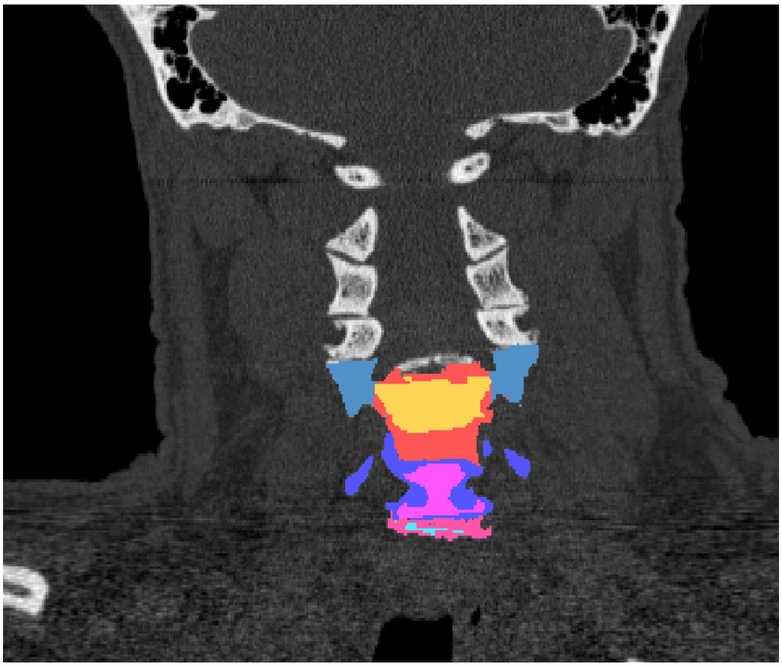

Figure 17: Coronal view of the painted masks.

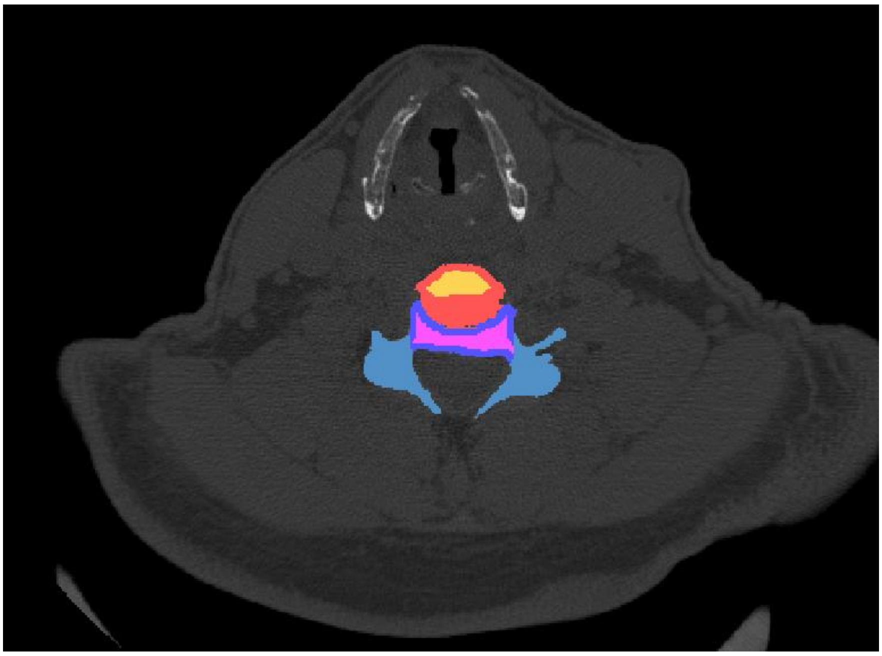

Figure 18: Axial view of the painted masks.

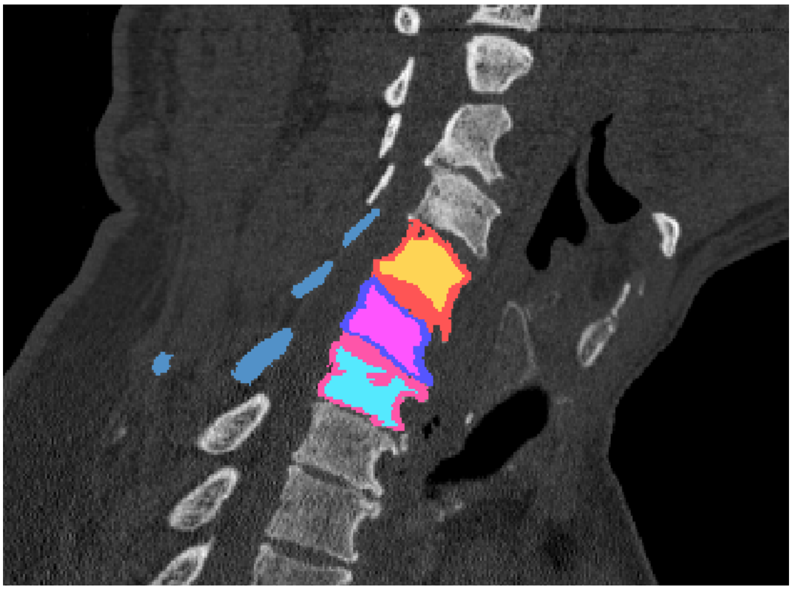

Figure 19: Sagittal view of the painted masks.

Once the 3D model generated by the painted parts, it is calculated by the same program using parameters that avoid smoothing the model (in order not to lose too much detail since the images do not have a very high resolution) to obtain a final 3D model (.stl) which is going to be imported to ICEM.

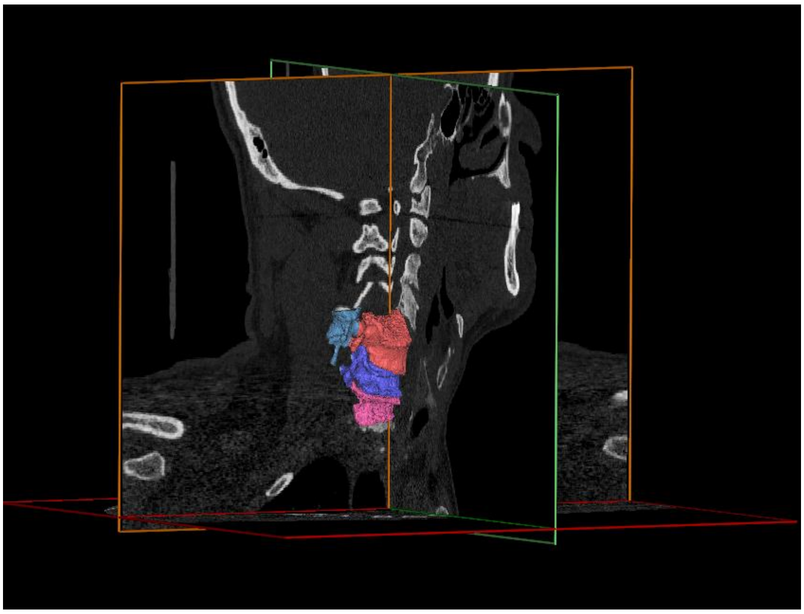

Figure 20: 3D model into CT images perspective

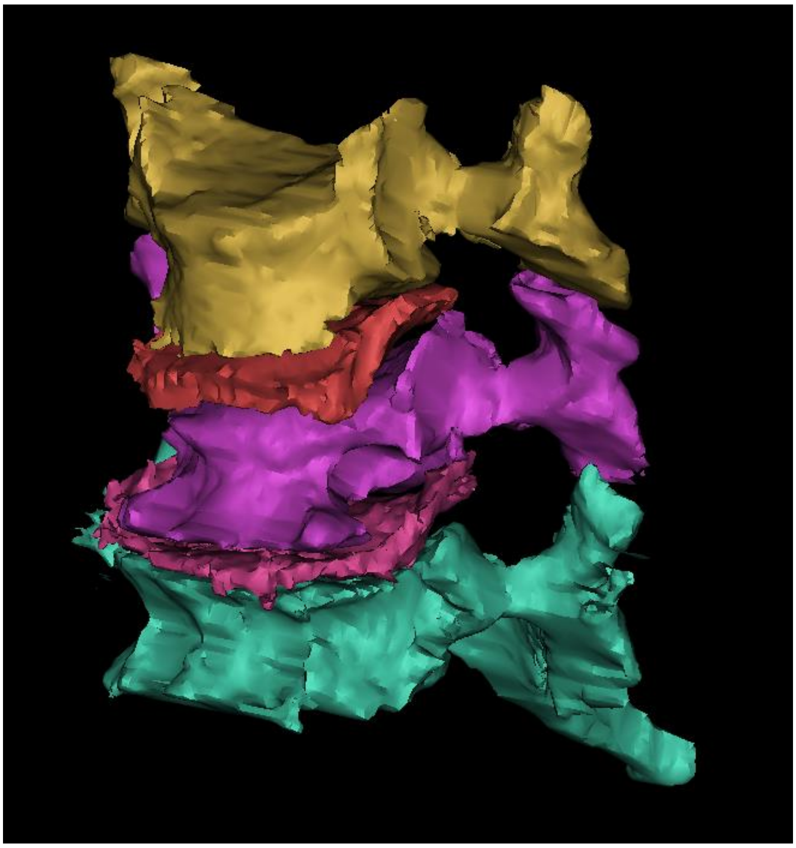

Figure 21: Preview masks without cortical bone

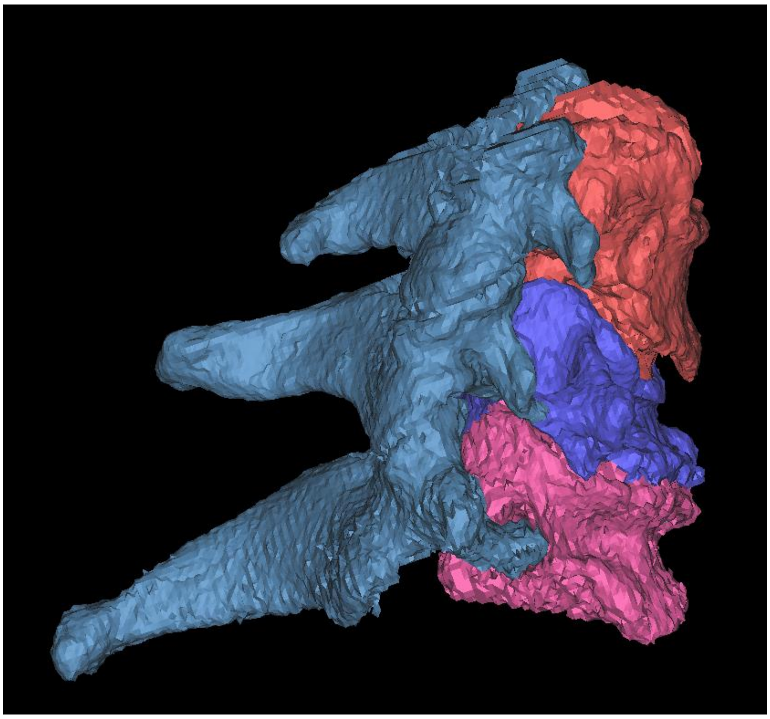

Figure 22: Preview masks with cortical bone

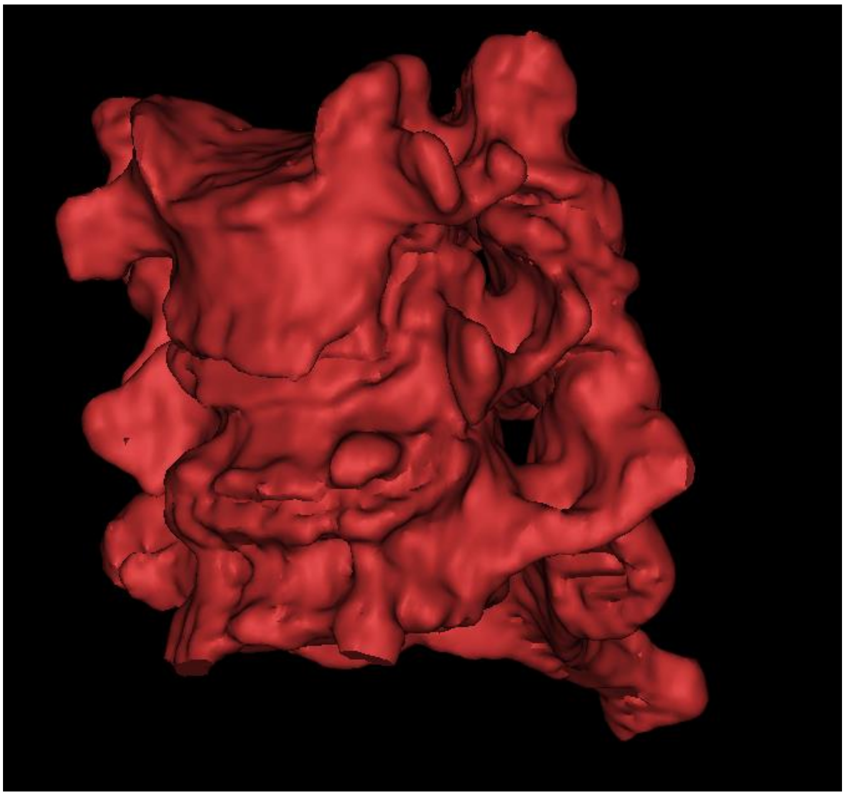

Figure 23: Final 3D model generated by Mimics

2.3.3 Mesh of the 3D Model of the cervical vertebrae

Once the model (.stl) is obtained, it is imported into the ICEM program to generate a mesh. Figure 23. A suitable configuration was used to generate a large number of polygons in the mesh to obtain better quality in the finite element analysis. Once the mesh is generated, the ICEM program allows exporting in a format compatible with Abaqus (.imp). Also, it was considered that it is better to use triangular structures for the meshing since this feature gives the triangular edge elements a great advantage when general, unstructured meshes are considered (Wu & Lee, 1997).

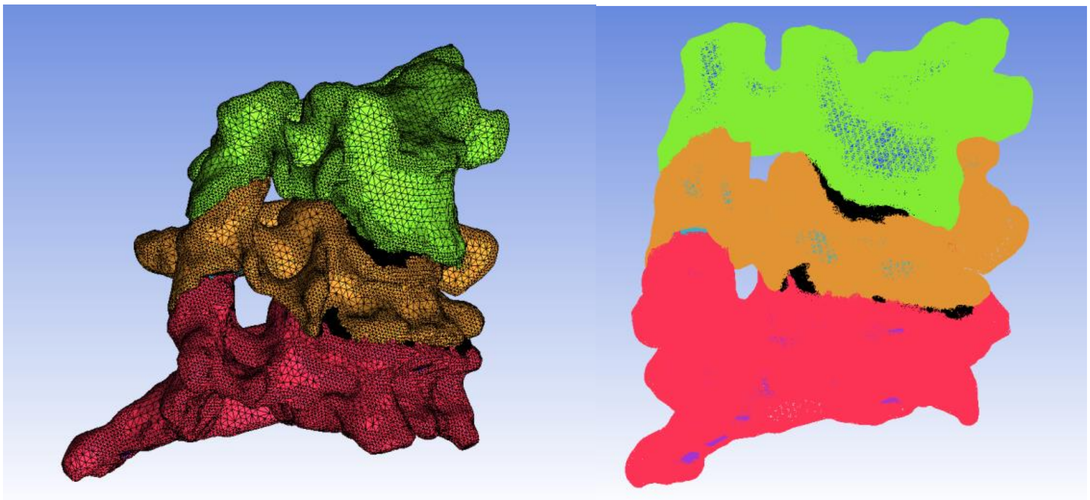

Figure 24: Mesh Generated by ICEM.

Note: The parameters of the mesh can be found on Annex 1 – Table 1.

2.3.4 Mesh Optimization in Mimics

Through Mimics, it is possible to generate an ideal mesh of the generated 3D model, which can be modified in such a way that the polygons have an optimal size. To do this, once the mesh is generated, it goes through a smoothing stage.

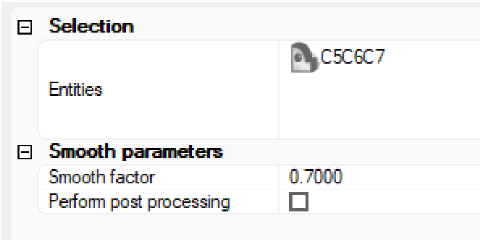

Figure 25: Smooth Parameters.

After smoothing, it can be seen that the quality of most of the elements is above 0.5 (Figure 17), which means that the mesh has a good quality according to Mimics. Using the "quality preserving reduce triangles tool" inside Mimics, it is expected to get a good result with the high-quality mesh to further reduce the number of triangles, resulting in a faster calculation time in the FEA solver program. Nevertheless, since the low resolution of the CT images, a large number of elements will be reduced which is beneficial for the calculation. According to Mimics certain characteristics must not exceed certain values for the analysis to be successful. These characteristics are maximum face angle, edge ratio, maximum face angle, aspect ratio, Jacobian. Furthermore, if the mesh does not surpass those thresholds, it is assumed that there are not going to be errors later. Finally, a volume mesh is generated to fill the surface mesh of the model. Figure 26 and Figure 27.

Figure 26: Quality of the Mesh – Histogram.

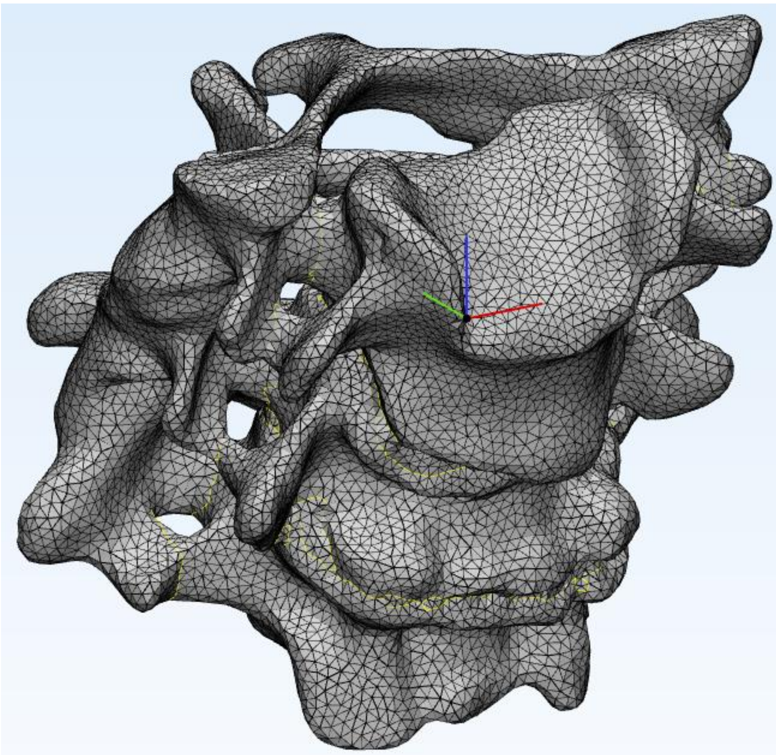

Figure 27: Final Mesh.

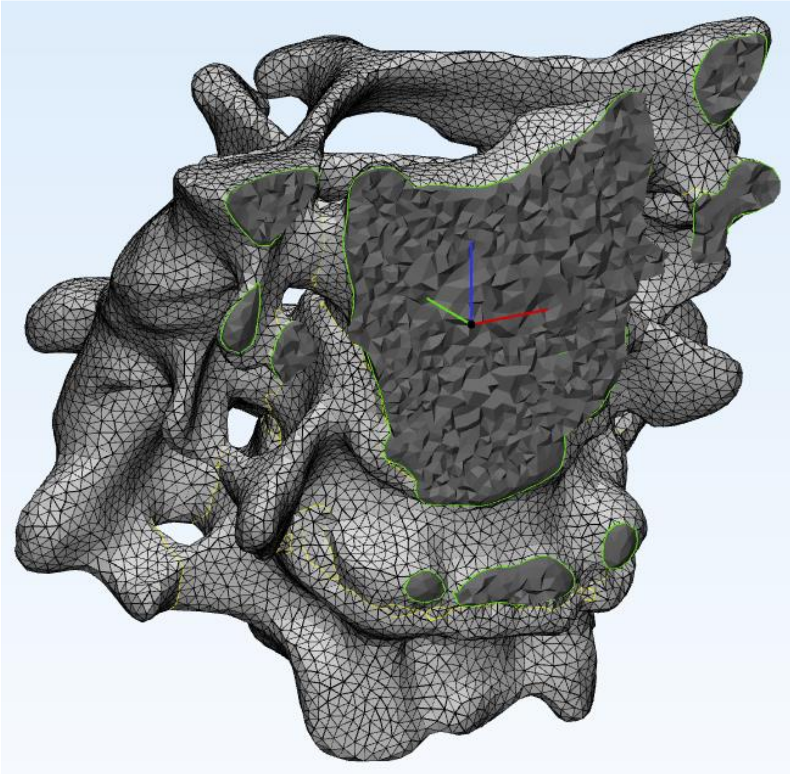

Figure 28: Volume Mesh.

2.3.5 Finite Element Analysis

The finite element analysis was carried out in Abaqus. For this purpose, the previously generated mesh was imported. Figure 28. According to Doğru (2018), it is mention that vertebrae have linearly elastic-isotropic behavior and their mechanical properties were described by Young's modulus and Poisson's ratio. The material properties used in the current cervical vertebra model are determined according to the Table 2. According to Doğru (2018) & Zhang et al., (2006) it is used compression force of 50N on the superior surface of the C5 endplate for the analysis. Furthermore, the bottom of the C7 surface was fixed in all directions. Figure 29. Finally, the pneumatocysts mesh were left as empty spaces because on the CT images there is no presence of liquid. Figure 6 and Figure 7.

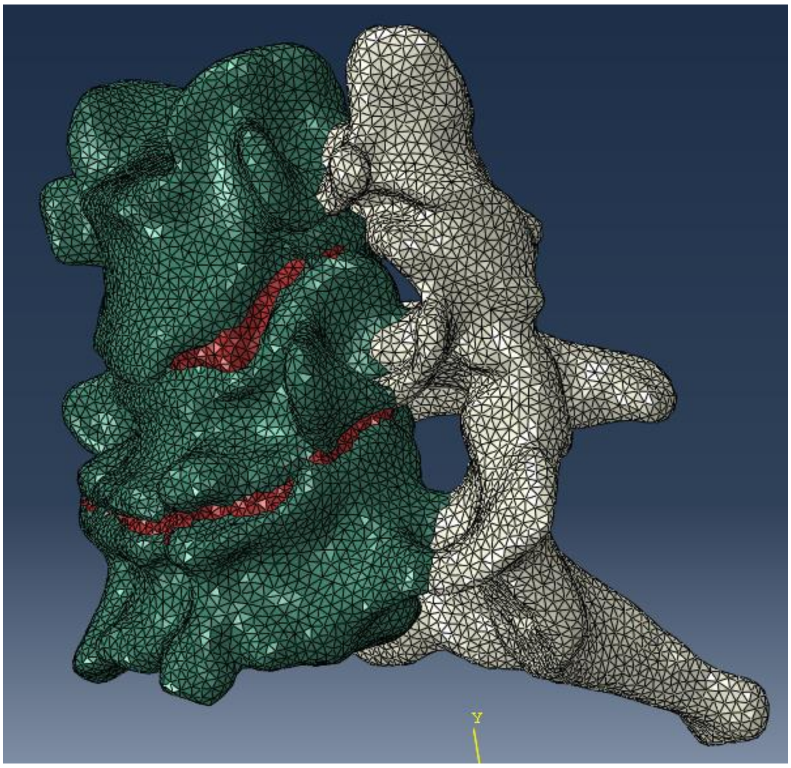

Figure 29: Imported mesh.

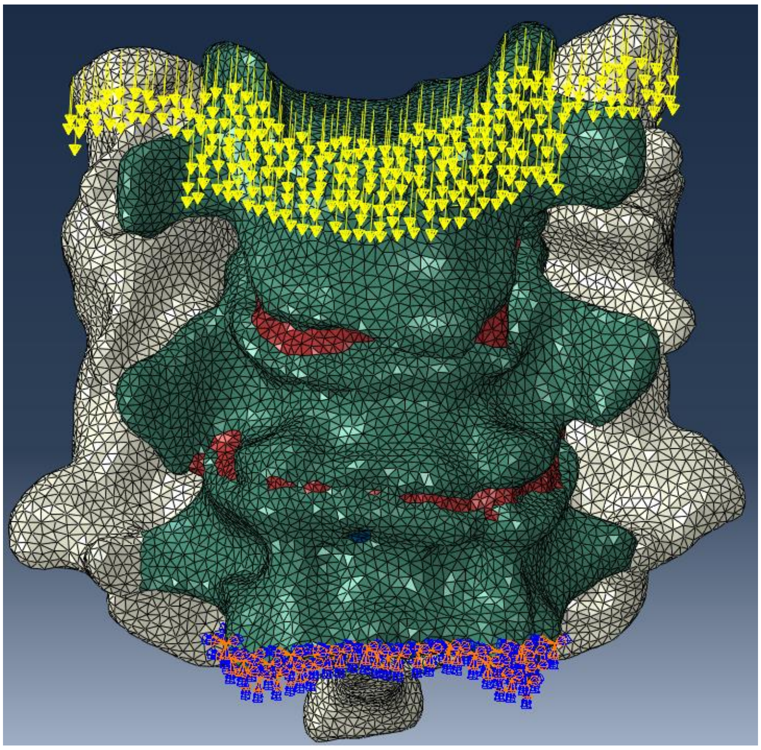

Figure 30: Load 50N & Boundary condition

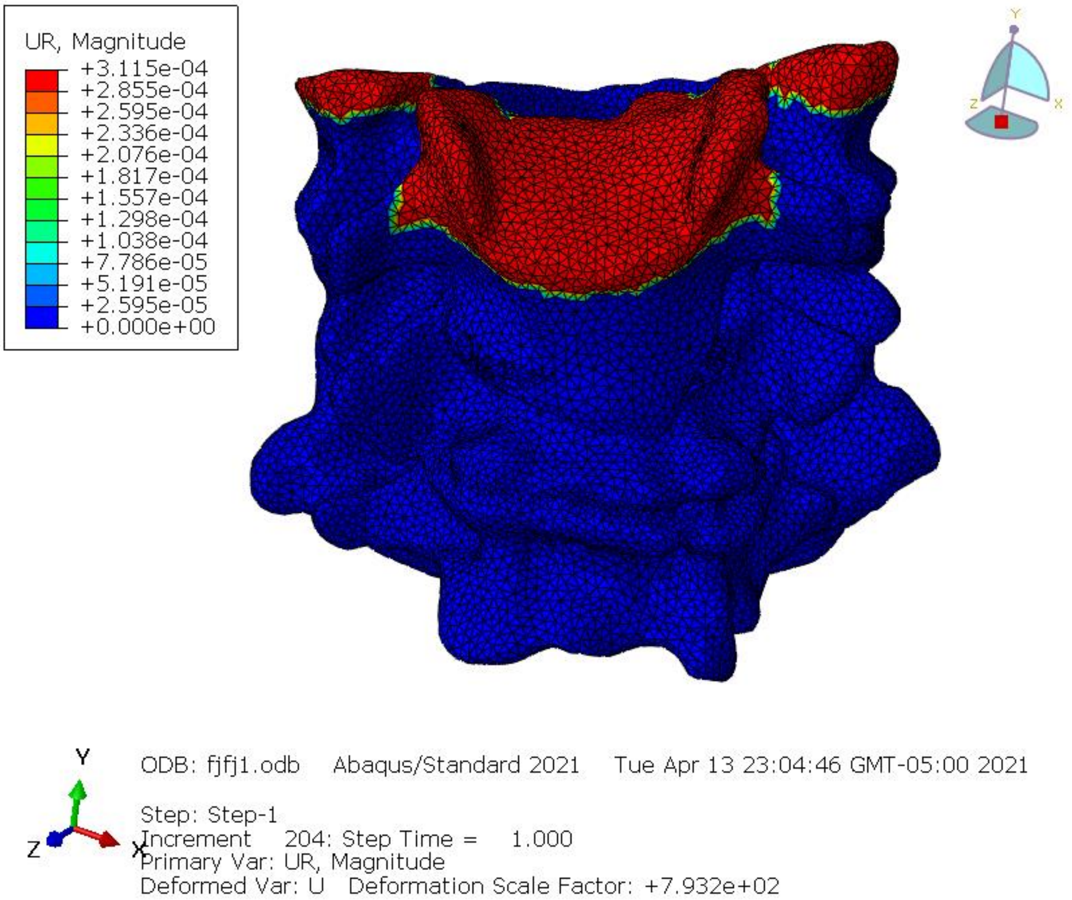

Figure 31: Load pressure points

Table 2: Material Properties

Material	***Young's Modulus (MPa)***	***Poisson's Ratio***	***References***
Cancellous Bone	450	0.29	(Cai et al., 2019), (Zhang et al., 2006), (Kumaresan et al., 1999)
Cortical Bone	10000	0.29	(Cai et al., 2019), (Ng et al., 2003), (Kumaresan et al., 1999)
Intervertebral Discs	1	0.49	(Smit et al., 1999). (Ng et al., 2003), (Zhang et al., 2006)
Posterior Element	3500	0.29	(Cai et al., 2019). (Ng et al., 2003), (Zhang et al., 2006), (Kumaresan et al., 1999)
Intervertebral Discs	1.66	0.4	(Ruberté et al., 2009)

Note: Characteristics of the materials used on the FEA.

Chapter III: Results

In this section you will find the data obtained from the FEA. These data are obtained from the simulation of the meshing in 3D. In addition, the deformation of the C5 vertebra will be obtained visually by the load of 50N previously applied. Figures 31. 32. 33. 34.
The mesh density consisted of 83629 nodes and 471612 Total number of elements. Also, 471612 linear tetrahedral elements of type C3D4. The final mesh density of each element is given in Table 3. Finally, the analysis took 205 frames to complete.

Table 3: Number of elements of each section

Part	***Number of elements***
C5 Cortical	41391
C5 Cancellous	35325
C6 Cortical	44591
C6 Cancellous	35592
C7 Cortical	47467
C7 Cancellous	48395
Intervertebral Disk C5-C6	14265
Intervertebral Disk C6-C7	12699
Posterior Elements	191887

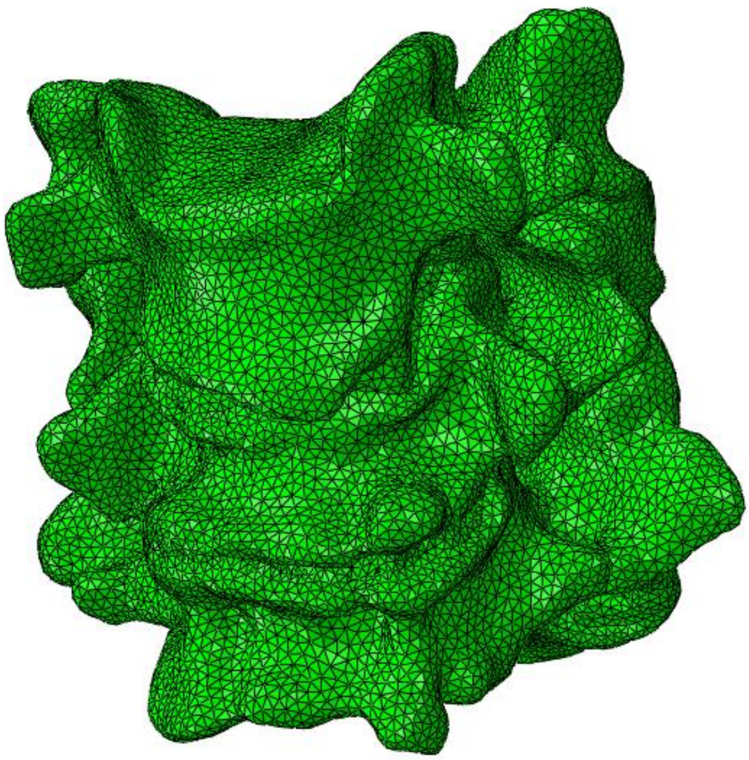

Figure 32: Front - Initial state of the vertebrae - FEA

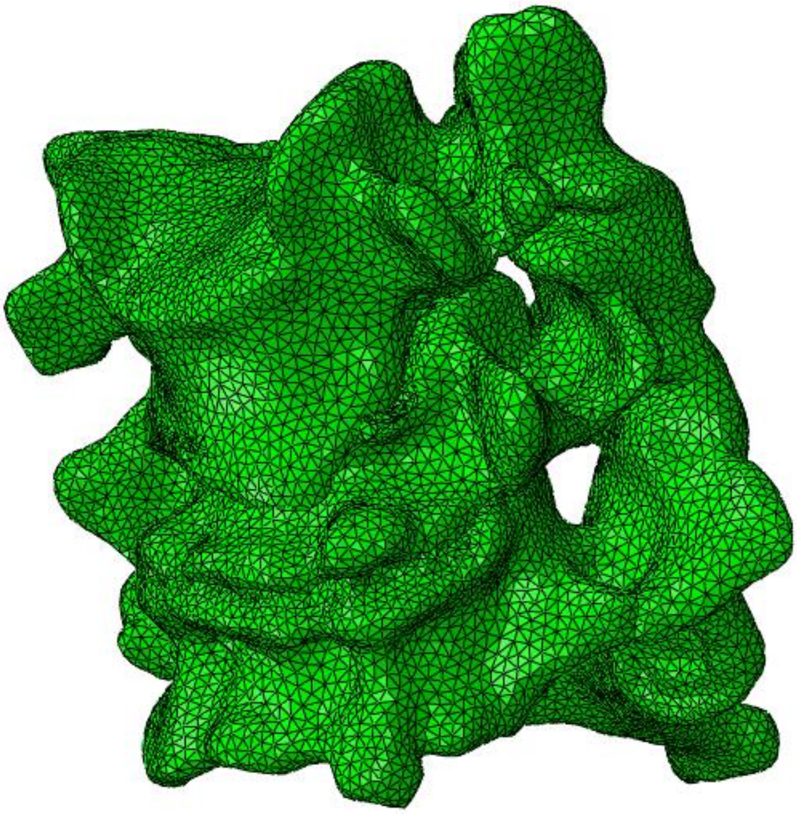

Figure 33: Front - Deformation state of the vertebrae - FEA

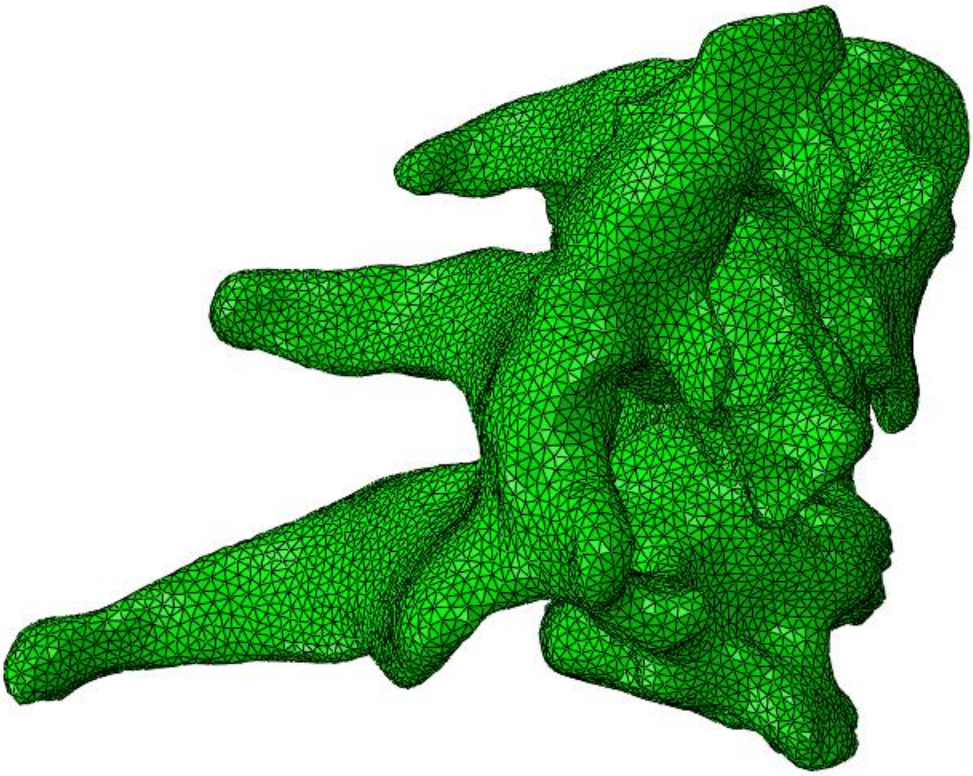

Figure 34: Side - Deformation state of the vertebrae - FEA

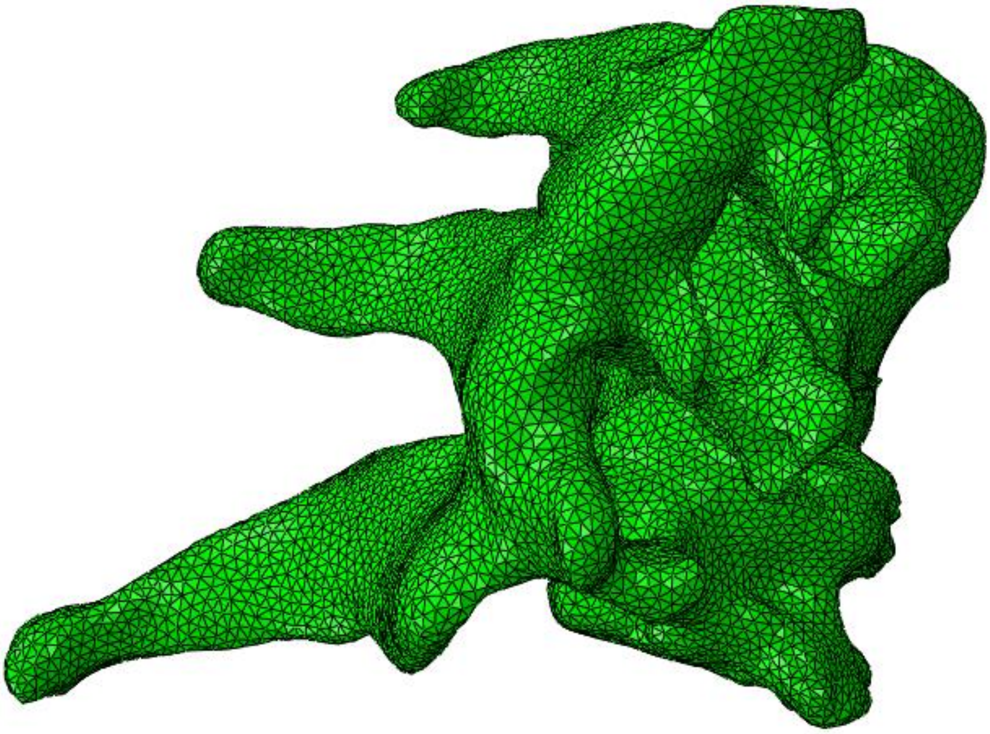

Figure 35: Side - Deformation state of the vertebrae – FEA

Von Mises stresses were evaluated according to the results obtained from FEA and the maximum stress over the intervertebral disc was given by Fig 35. The maximum von Mises stresses were observed during flexion and it was calculated for severely degenerated intervertebral disc (MPa). In order to obtain the history curves, it was used the guide from Abaqus (Abaqus-docs, n.d.). For the severely degenerated intervertebral disc, the maximum stress in flexion was 0.0049MPa.

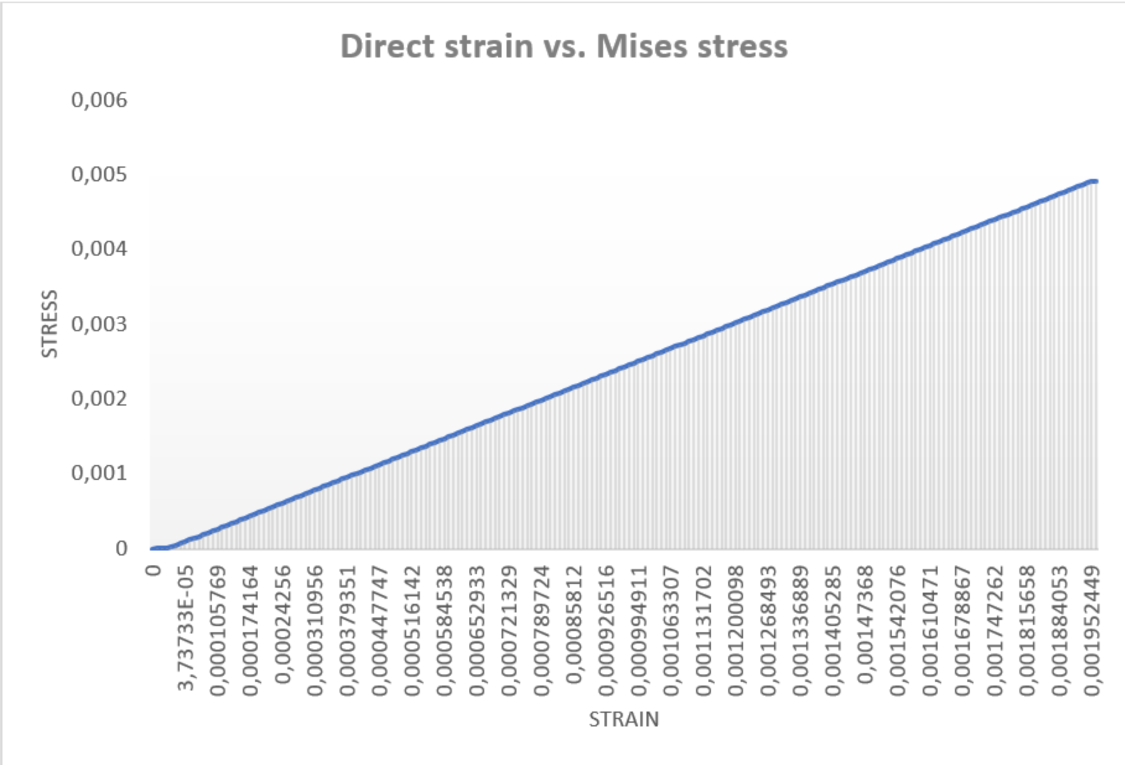

Figure 36: Stress vs Strain of one node inside of the intervertebral disk C5. Data of the table can be found in Annex 2- Figure 1, Figure 2, Table 2.

The displacement data of a node of the intervertebral disc C5 in the X, Y, Z axes were obtained. Fig 35. The Figure 37 shown the max displacement in the X-axis is 0,002565188m; the Figure 38 shown that the max displacement in the Y-axis is 0,008033744m, and the figure 39 shown that the max displacement in the Z-axis is 0,002203539m.

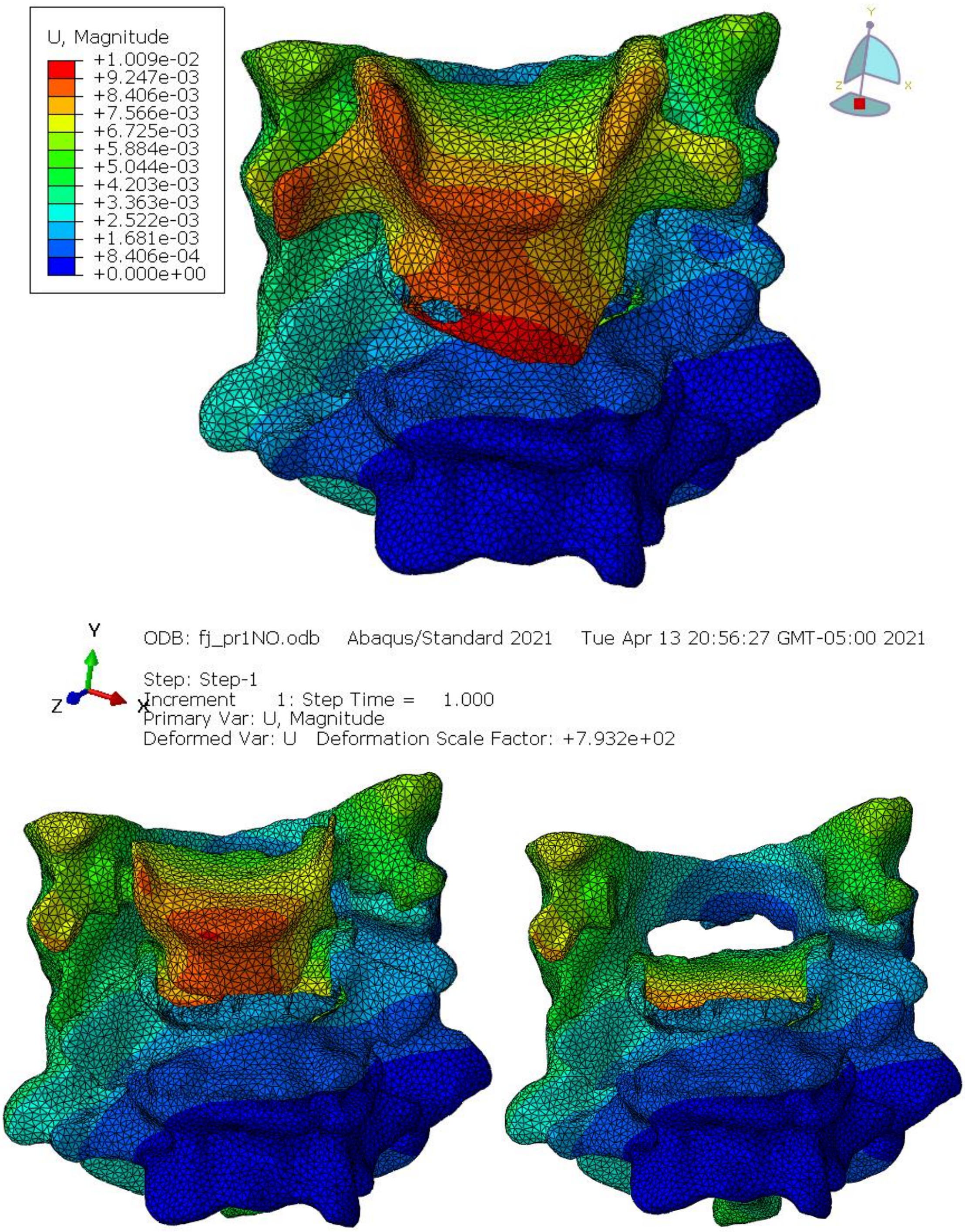

Figure 37: Displacement of the nodes of the model.

Notes: Yellow to Red nodes more displaced. The intervertebral disk is displaced more on the front side.

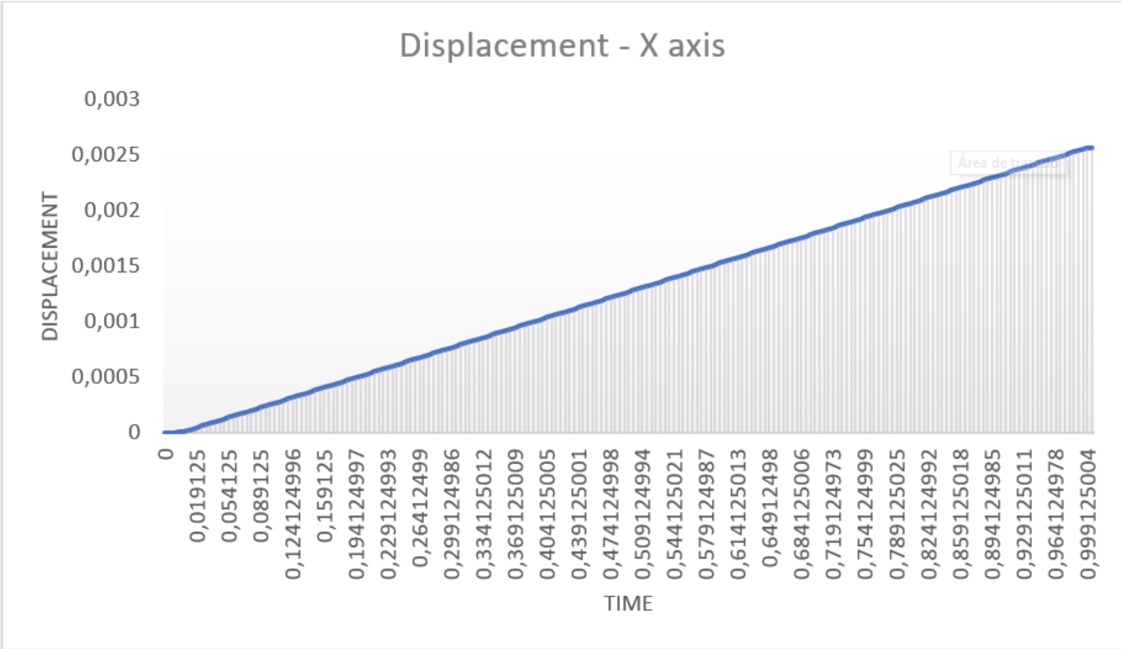

Figure 38: X-axis displacement of one node inside of the intervertebral disk C5. Data of the table can be found in Annex 3 – Figure 3, Table 3.

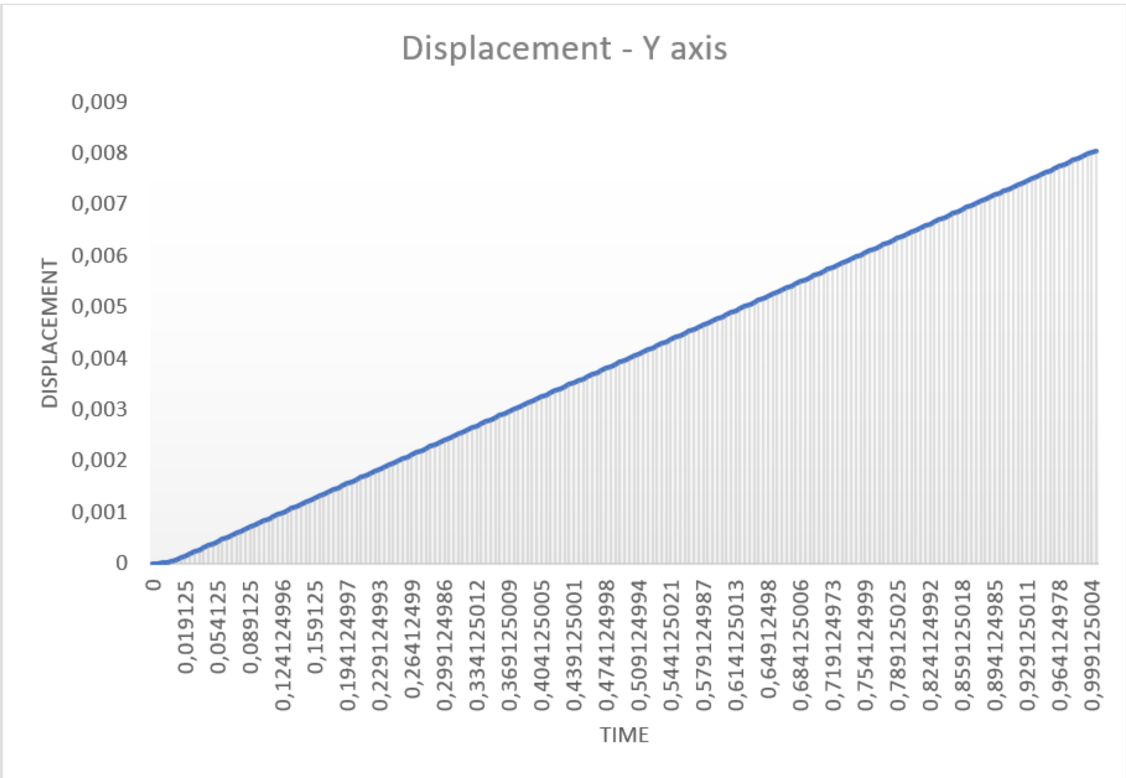

Figure 39: Y-axis of one node inside of the intervertebral disk C5. Data of the table can be found in Annex 4 – Figure 4, Table 4.

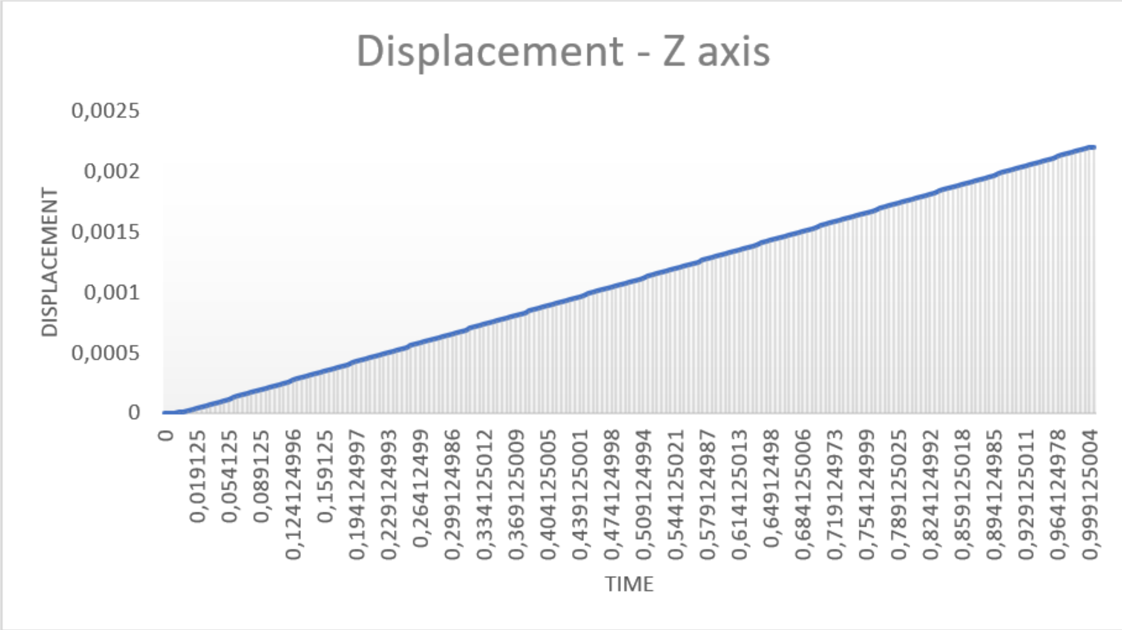

Figure 40: Z-axis of one node inside of the intervertebral disk C5. Data of the table can be found in Annex 5 – Figure 5, Table 5.

The pressure data were obtained through an integration point (polygon) not of the intervertebral disk but the adjacent bone. the load. Figure 37 and Figure 38. The data can be found in Annexes – Annex 6.

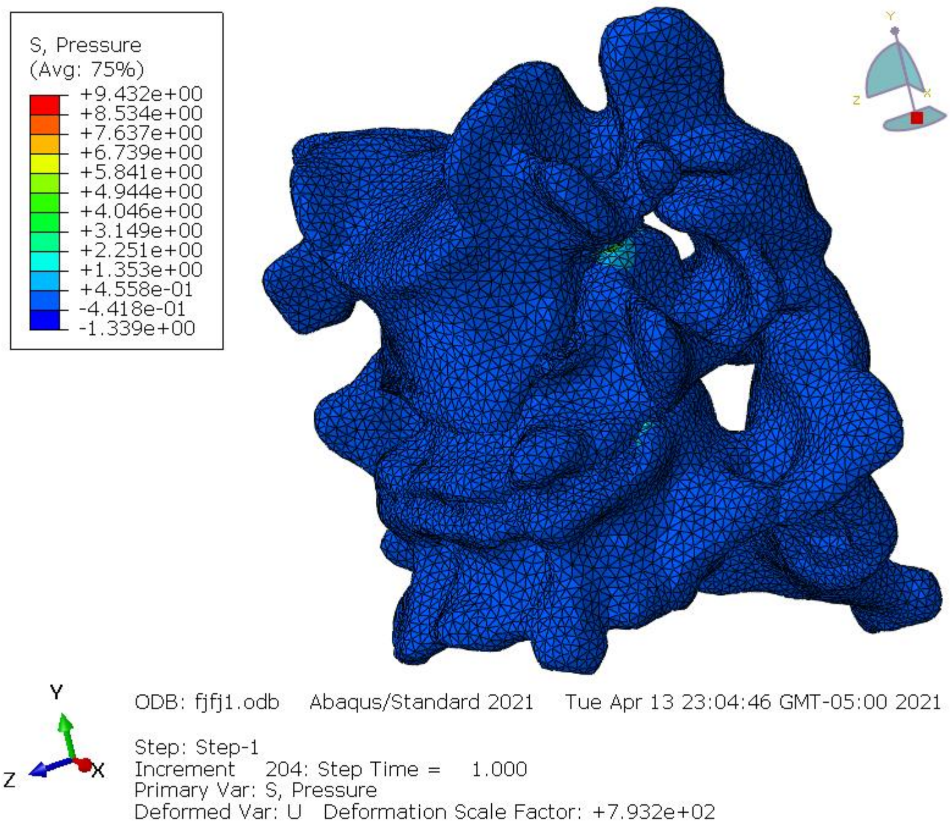

Figure 41: Pressure points on the C6 vertebra

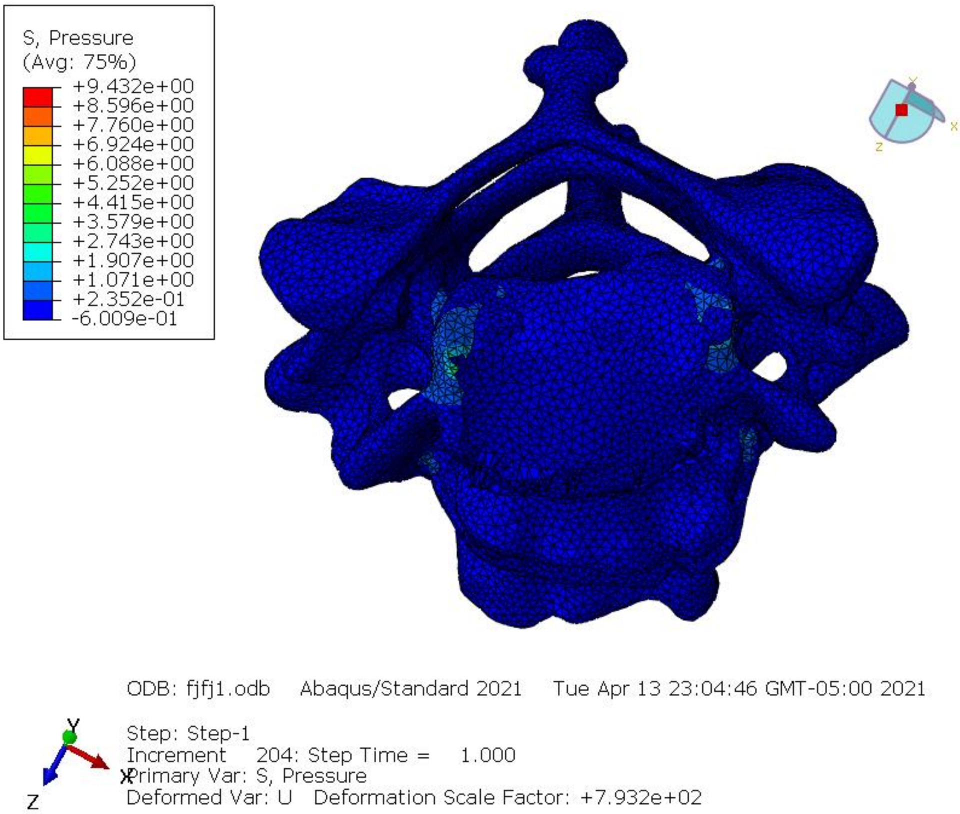

Figure 42: Pressure points on the C6 vertebra – Top view

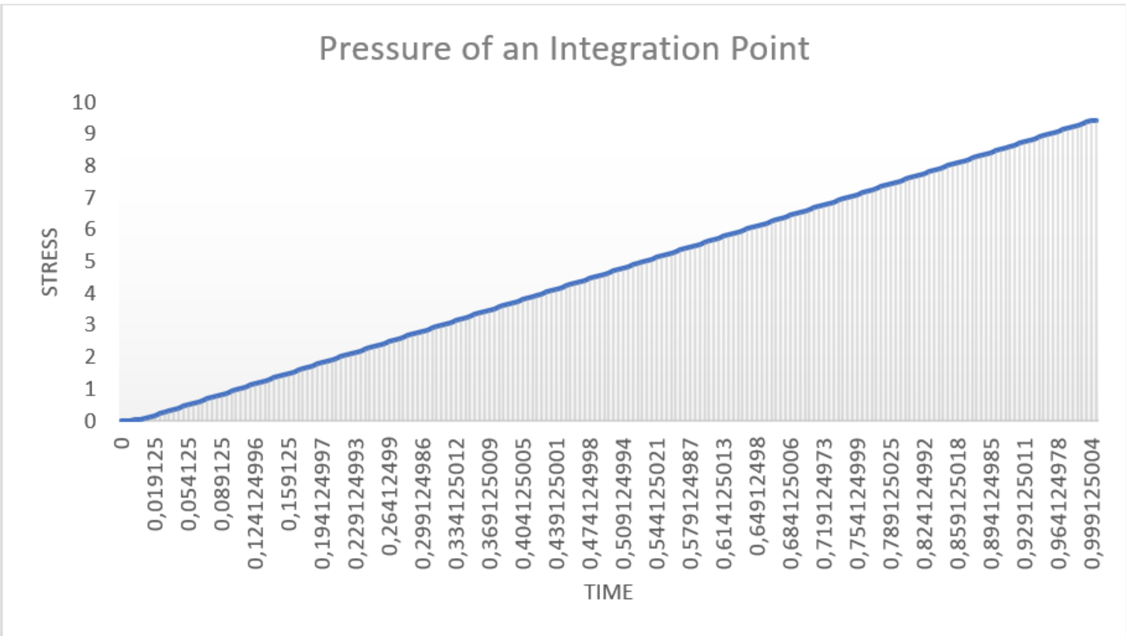

Figure 43: Z-axis of one node inside of the intervertebral disk C5. Data of the table can be found in Annex 6 – Table 6.

Table 4: Minimum Safety Factor

Position	*Minimum Safety Factor*
For seated position	93.9
For standing position	102.04
For lying prone	18.57

Note: To calculate the safety factor it was used the minimum strength value of the three positions.

3.1 Discussion

The end plates were not modeled because the CT images does not show that the end plates of the patient were there. The deterioration of the endplates may be due to disc herniation, due that disk herniation is the most common disk disorder. This is caused by the bulge or rupture of the discs (either partially or totally) posteriorly or posterolaterally, and press on the nerve roots in the spinal canal (Urban & Roberts, 2003).

The material property of the annulus fibrosus was previously assigned as hyperelastic material, using the coefficient of Mooney-Rivlin hyperelastic material described as C10=1.8, C01=0.45, D1=1e-10 for severe annulus (Doğru, 2018). Nevertheless, the output of the analysis cannot be completed due to an error of this data. For this reason, the analysis was carried out as if the intervertebral discs are isotropic-elastic material.

There are two ways to apply the load on the mesh. The first one is a force load with continuum distributing and coupling constraint. The second one is load under pressure. It is considered that a similar result will be obtained from either of the two ways of applying a load. (*Pressure VS Concentrated Force Comparison (with Continuum Distributing Coupling) in Finite Element Analysis | y-Chen*, n.d.). Therefore, in this FEA it is used pressure for applying the load.

According to the data of Doğru (2018), the stress increased nearly ten-fold with the severely degenerated model. This can be visualized with the results of this model. In figure 33 and figure 35, it is shown that the severely degenerated intervertebral disk is severely compressed. Therefore, is receiving more stress. Nevertheless, the vertebrae are appeasing some of the stress of the intervertebral disk. Figure 42.

According to the analysis of Pressure of an Integration Point on the vertebra, it is observed that the intervertebral disc does not calm the pressure exerted by the bone, rather it is observed that the C5 vertebra collides with the C6 vertebra and the C6 vertebra collides with the C7 vertebra. Figure 41 and Figure 42.

In the FEA of Doğru (2018), Lewis (2016), Gandhi et al. (2019) & Goel & Clausen (1998) the models have been modeled from the healthy intervertebral discs. In contrast to the model of this study, the intervertebral disks of the authors are capable of bear the force of the bone, in other words, the vertebras don’t collide with each other.

In the FEA from Doğru (2018) the analysis for the degenerated intervertebral disc was made using a normal size intervertebral disc but changing the material properties. In this study, the intervertebral size was less, and the material properties also were different due to previously commented errors of the analysis. Therefore, it is expected to have different results.

Doğru (2018) reported that the height of intervertebral disks reduced as the degeneration progressed. In other words, it means that increasing stress cause the decreasing height of intervertebral disks as the degeneration progressed. The model used in this FEA have short intervertebral disk (this can be due to the age of the patient, and also due for the job o the patient). Therefore, the stress caused by the different daily activities can cause the decreasing of height of the intervertebral disks.

Goel & Clausen's (1998) and Kumaresan et al. (1999) analysis is focused on the movements of the vertebrae. According to their analysis, in order to predict the movement of vertebrae, it is necessary that the intervertebral disks are not damaged. In contrast to this FEA, the movement is limited because there is no room for the normal displacement of the vertebrae due to the severely damaged intervertebral disks. Furthermore, according to the studied model, the patient should have pain when some movement is in action. Furthermore, it is important to simulate tendons and muscles in order to achieve a more realistic simulation.

The analysis simulation suggests that degeneration of the intervertebral discs affects the whole spine (during flexion motion). The loss of proteoglycan in degenerate discs has a major effect on the disc’s load-bearing behavior (Urban & Roberts, 2003). Also, the load may thus lead to inappropriate stress concentrations along the endplate or in the annulus (Urban & Roberts, 2003). The nucleus normally carries a portion of external loading and supports the annulus (Juan et al., 2018). Due to degeneration, the nucleus cannot support the stress to external loading and as a consequence, the stress in annulus increased as the degeneration progressed.

Panzer & Cronin's (2009) and Ng et al. (2003) analysis, the compression of healthy intervertebral discs of cervical vertebrae was studied. In the case of the FEA of the generated 3d mesh, was not possible to analyze the compression forces due to the size of the intervertebral disc and also of the collision of the vertebrae. Furthermore, the material properties of the severely damaged intervertebral discs cause clipping and deformation in the analysts when a bigger load is applied.

According to the analysis, a displacement of the intervertebral disc was observed through the flexion, which suggests the appearance of herniated discs (*Hernia Discal: MedlinePlus Enciclopedia Médica*, n.d.). According to Y. Aroche Lafargue et al, the risk factors related to the presence of herniated discs in the spine stand out: obesity, age, occupation (jobs with prolonged standing). Over 45 years of age, degenerative disc or facet joint lesions predominate. The prevalence of herniated disc is in the range of 1-3% of back pain, in addition to the fact that males are the most affected by herniated discs (Aroche Lafargue et al., 2015). Furthermore, the simulation has also shown that at the moment of flexion the osteophyte of the C5 vertebra collides with the C6 vertebra.

Rigidity is observed between vertebrae C6 and C7, according to the simulation it can be concluded that there is a bone weld between the two vertebrae. In addition, displacement of posterior elements is observed, which causes compression of the nerve due to the displacement of the vertebral foramen. Between the C6 and C7 vertebrae, it is observed that there is contact between the bones since the intervertebral disc is worn. Spondylo-arthrosis is observed between C6 and C7 in addition to the fusion of the two vertebrae, if the bone collides with bone, the cartilage between the vertebrae wears out. When cartilage is damaged, a bone-to-bone collision occurs and, as it is a rheumatic disease, inflammation occurs in the bone and cartilage. This causes some ramifications to be produced that later calcify, which produces osteoarthritis. These problems can be seen on CT scans.

The safety factor is defined as the ratio between the strength of the material and the maximum stress in the part (Cyprien, 2016). When the stress in a specific position becomes superior to the strength of the material, the safety factor ratio becomes inferior to 1, this when there is danger. According to (Newell et al., 2017) in a healthy lumbar disc, in vivo pressures in the nucleus are between 460 and 1330 kPa in the seated position, 500 and 870 kPa in the standing position, and 91 and 539 kPa when lying prone. Then, taking the data of the Figure 32, the stress max is 0.0049MPa/4.9 kPa. According to the data of the Table 4, every value of safety factor is above 1 it is concluded that model is safe.

3.2.1 Limitations

The model was generated in a low resolution. Also, the model is not entirely on the X-axis but is between the X and Z axes. To solve that, it was necessary to rotate the coordinates manually on Abaqus.

When a reference point for the load of 50N was used (figure 44), it was observed that the analysis ended without any error, however, the simulation showed the same results as if there is no point of reference. In other words, the analysis succeeded on either way.

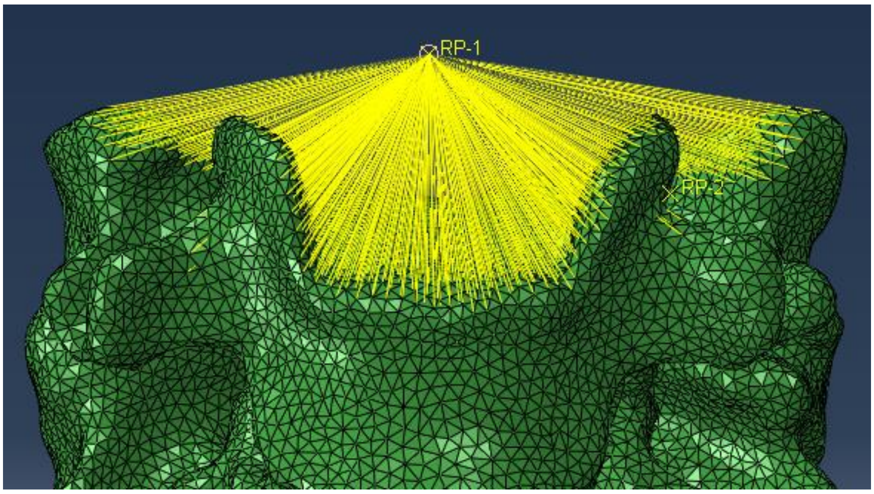

Figure 44: Reference point + load

It was obligatory to turn off the “Nigeom” option in order to have better results. It is also important to modify the time increment required to obtain better results in the plots.

There is not much FEA of severely damaged intervertebral disks.

Chapter IV: Conclusions

In a nutshell, FEA is widely used to analyze and study the quality of products or projects. The Finite Element Method allows obtaining answers for numerous problems of either engineering or biomechanical answers. Therefore, to obtain the best of the results the mesh mustn't surpass the thresholds of the maximum face angle, edge ratio, maximum face angle, aspect ratio, Jacobian. In other words, the mesh is the most important part of the analysis to achieve the best results. The mesh used for this analysis was taken from tomographic images of a 64-year-old patient with osteoarthritic and degenerative bone alterations, spondylosis deformans, decrease in the width of the intervertebral spaces, and asymmetry of the intervertebral spaces.

- A complete model of the C5, C6, and C7 vertebrae was developed using the finite element method implemented in the Abaqus program. The model was created using the MIMICS medical and ANSYS tools.

- The 3D model was created from the existing CT images in the Medical Imaging Databank of the Valencia Region using Mimics medical. The model is separated into cancellous bone, cortical bone, posterior elements and intervertebral discs.

- With the help of Mimics and Ansys, a mesh was created that was exported and imported to be used in Abaqus. Each part was defined with a Poisson coefficient and elastic moment depending on the material.

- The behavior of the C5 intervertebral disc under the action of the 50N load was studied. The deformation, tension, stress and pressure have been obtained.

- In general, excess weight, trauma, jumping, or due to a whiplash can cause problems in the spine. Regarding the model carried out in this study, it can be concluded that when performing the analysis with the intervertebral discs with a smaller volume compared to other studies, the results of Stress will be different.

- However, it is important to have a more realistic perspective for an FEA. Being the model generated from a patient, the behavior of the different pathologies can be observed in a 3D environment to better understand the biological and biomechanical behavior of the cervical vertebrae.

Chapter V: References

1. *A Quick Overview of ICEM*. (n.d.). Retrieved April 5, 2021, from http://hmf.enseeiht.fr/travaux/CD0001/travaux/optmfn/micp/reports/s14imt2/aqooi.htm
2. Abaqus-docs. (n.d.). *Postprocessing the results*. Retrieved April 13, 2021, from https://abaqus-docs.mit.edu/2017/English/SIMACAEGSARefMap/simagsa-c-matpostprocess2.htm
3. *ABAQUS software de analisis y simulacion CAE*. (n.d.). Retrieved April 5, 2021, from https://www.3dcadportal.com/abaqus-simulia.html
4. Adams, M. A., & Roughley, P. J. (2006). What is intervertebral disc degeneration, and what causes it? *Spine*, *31*(18), 2151–2161. https://doi.org/10.1097/01.brs.0000231761.73859.2c
5. Altman, R., Asch, E., Bloch, D., Bole, G., Borenstein, D., Brandt, K., Christy, W., Cooke, T. D., Greenwald, R., Hochberg, M., Howell, D., Kaplan, D., Koopman, W., Longley, S., Mankin, H., McShane, D. J., Medsger, T., Meenan, R., Mikkelsen, W., … Wolfe, F. (1986). Development of criteria for the classification and reporting of osteoarthritis: Classification of osteoarthritis of the knee. *Arthritis & Rheumatism*, *29*(8), 1039–1049. https://doi.org/10.1002/art.1780290816
6. Aroche Lafargue, Y., Pons Porrata, L. M., De La Cruz De Oña, A., & González Ferro, I. (2015). Pathogenia, clinical pattern, and imagenologic diagnosis through magnetic resonance of the disc herniation. *Medisan*, *19*(3), 391–402. http://scielo.sld.cu/scielo.php?script=sci_arttext&pid=S1029-30192015000300012
7. Bakkum, B. W. (2013). Surface Anatomy of the Back and Vertebral Levels of Clinically Important Structures. In *Clinical Anatomy of the Spine, Spinal Cord, and ANS* (Third Edit). Elsevier Inc. https://doi.org/10.1016/B978-0-323-07954-9.00001-3
8. Bibhuti Bhusan-Das, Salim Barbhuiya, Rishi Gupta, P. S. (2019). *Recent Developments in Sustainable Infrastructure Select Proceedings of ICRDSI 2019*. http://www.springer.com/series/15087

9. *BIMCV – Medical Imaging Databank of the Valencia Region*. (n.d.). Retrieved July 11, 2021, from https://bimcv.cipf.es/

10. Bogduk, N. (2016). Functional anatomy of the spine. In *Handbook of Clinical Neurology* (1st ed., Vol. 136). Elsevier B.V. https://doi.org/10.1016/B978-0-444-53486-6.00032-6

11. Bogduk, N., & Mercer, S. (2000). Biomechanics of the cervical spine. I: Normal kinematics. *Clinical Biomechanics*, *15*(9), 633–648. https://doi.org/10.1016/S0268-0033(00)00034-6

12. Cai, X. Y., Sun, M. S., & Du, C. F. (2019). The Biomechanical Response of Cervical Spine under Different Follower Loads. *Proceedings of 2019 IEEE International Conference on Mechatronics and Automation, ICMA 2019*, 360–364. https://doi.org/10.1109/ICMA.2019.8816441

13. Cyprien. (2016, December 26). *Safety factor: How do I calculate that? - FEA for All*. https://feaforall.com/calculate-safety-factor/

14. Doğru, S. C. (2018). Nonlinear Finite Element Analysis of Intervertebral Disc: a Comparative Study. *Sakarya University Journal of Science*, *October*, 1–1. https://doi.org/10.16984/saufenbilder.305347

15. Gandhi, A. A., Grosland, N. M., Kallemeyn, N. A., Kode, S., Fredericks, D. C., & Smucker, J. D. (2019). Biomechanical analysis of the cervical spine following disc degeneration, disc fusion, and disc replacement: A finite element study. *International Journal of Spine Surgery*, *13*(6), 491–500. https://doi.org/10.14444/6066

16. García Reyes, L. E. (2013). Materialise NV. *Journal of Chemical Information and Modeling*, *53*(9), 1689–1699. https://www.accessdata.fda.gov/cdrh_docs/pdf18/K183105.pdf

17. Goel, V. K., & Clausen, J. D. (1998). Prediction of load sharing among spinal components of a C5-C6 motion segment using the finite element approach. In *Spine* (Vol. 23, Issue 6, pp. 684–691). https://doi.org/10.1097/00007632-199803150-00008

18. *Hernia discal: MedlinePlus enciclopedia médica*. (n.d.). Retrieved April 13, 2021, from https://medlineplus.gov/spanish/ency/article/000442.htm

19. Husain, M. A., Tetradis, S., & Mallya, S. M. (2015). Intraosseous pneumatocysts of the cervical spine: A report of four cases and review of literature. *Oral Surgery, Oral Medicine, Oral Pathology and Oral Radiology*, *119*(1), e49–e54. https://doi.org/10.1016/j.oooo.2014.09.019

20. Juan, I., Lozano, L., Dávila, C., Mora, J., & Tramontini, C. (2018). Anatomía de la columna vertebral en radiografía convencional. *Revista Médica Sanitas*, *21*(1), 39–46. https://doi.org/10.26852/01234250.11

21. Kumaresan, S., Yoganandan, N., & Pintar, F. A. (1999). Finite element analysis of the cervical spine: A material property sensitivity study. *Clinical Biomechanics*, *14*(1), 41–53. https://doi.org/10.1016/S0268-0033(98)00036-9

22. Levyakov, S. V. (2011). Invariant-based geometrically nonlinear formulation of a triangular finite element of laminated shells. *Advanced Structured Materials*, *15*, 329–354. https://doi.org/10.1007/978-3-642-21855-2_23

23. Lewis, G. (2016). Finite Element Analysis Study of the Influence of Simulated Surgical Methods on Kinematics of a Model of the Full Cervical Spine. *Spine Research*, *02*(01), 1–9. https://doi.org/10.21767/2471-8173.100014

24. Mahadevan, V. (2018). Anatomy of the vertebral column. *Surgery (United Kingdom)*, *36*(7), 327–332. https://doi.org/10.1016/j.mpsur.2018.05.006

25. Menchetti, P. P. M. (2015). Cervical spine: Minimally invasive and open surgery. *Cervical Spine: Minimally Invasive and Open Surgery*, 1–251. https://doi.org/10.1007/978-3-319-21608-9

26. Moore, R. J. (2006). The vertebral endplate: Disc degeneration, disc regeneration. *European Spine Journal*, *15*(SUPPL. 3), 333–337. https://doi.org/10.1007/s00586-006-0170-4

27. Nakayama, T., Ehara, S., & Hama, H. (2001). Spontaneous progression of vertebral intraosseous pneumatocysts to fluid-filled cysts. *Skeletal Radiology*, *30*(9), 523–526. https://doi.org/10.1007/s002560100367

28. Newell, N., Little, J. P., Christou, A., Adams, M. A., Adam, C. J., & Masouros, S. D.

(2017). Biomechanics of the human intervertebral disc: A review of testing techniques and results. In *Journal of the Mechanical Behavior of Biomedical Materials* (Vol. 69, pp. 420–434). Elsevier Ltd. https://doi.org/10.1016/j.jmbbm.2017.01.037

29. Ng, H. W., Teo, E. C., Lee, K. K., & Qiu, T. X. (2003). Finite element analysis of cervical spinal instability under physiologic loading. *Journal of Spinal Disorders and Techniques*, *16*(1), 55–65. https://doi.org/10.1097/00024720-200302000-00010

30. Oliver, J., & Middleditch, A. (1991). Structure of the Vertebral Column. *Functional Anatomy of the Spine*, 1–58. https://doi.org/10.1016/b978-0-7506-0052-1.50004-3

31. Panzer, M. B., & Cronin, D. S. (2009). C4-C5 segment finite element model development, validation, and load-sharing investigation. *Journal of Biomechanics*, *42*(4), 480–490. https://doi.org/10.1016/j.jbiomech.2008.11.036

32. Park, J. H., Kim, S. W., Kim, H. S., & Ko, J. U. (2015). Rapid Resolution of Traumatic Pneumatocyst in the Cervical Spine: A Case Report. *Korean Journal of Spine*, *12*(2), 88. https://doi.org/10.14245/kjs.2015.12.2.88

33. Penning, L., & Wilmink, J. T. (1987). Rotation of the cervical spine: A CT study in normal subjects. In *Spine* (Vol. 12, Issue 8, pp. 732–738). https://doi.org/10.1097/00007632-198710000-00003

34. *Pressure VS Concentrated Force comparison (with Continuum Distributing Coupling) in Finite Element Analysis | y-chen*. (n.d.). Retrieved April 13, 2021, from https://yudhichen.wordpress.com/2017/06/29/pressure-vs-concentrated-force-comparison-with-continuum-distributing-coupling-in-finite-element-analysis/

35. Ramirez, H., Blatt, E. S., Cable, F., Mccomb, L., Zornoza, J., & Hibri, N. S. (1984). Intraosseous Ilium. *Radiology*, 503–505.

36. Ruberté, L. M., Natarajan, R. N., & Andersson, G. B. (2009). Influence of single-level lumbar degenerative disc disease on the behavior of the adjacent segments-A finite element model study. *Journal of Biomechanics*, *42*(3), 341–348. https://doi.org/10.1016/j.jbiomech.2008.11.024

37. Ruffoni, D., & Van Lenthe, G. H. (2017). 3.10 Finite element analysis in bone research: A

computational method relating structure to mechanical function. In *Comprehensive Biomaterials II* (Issue October). Elsevier Ltd. https://doi.org/10.1016/B978-0-12-803581-8.09798-8

38. Sen, D., Satija, L., Saxena, S., Rastogi, V., & Singh, M. (2015). Intraosseous pneumatocyst of the cervical vertebra. *Medical Journal Armed Forces India*, *71*(4), 380–383. https://doi.org/10.1016/j.mjafi.2013.10.003

39. Smit, T., Odgaard, A., & Schneider, E. (1999). *Structure and Function of Vertebral Trabecular Bone* (pp. 2823–2833). Department of Clinical Physics and Engineering. https://journals.lww.com/spinejournal/Abstract/1997/12150/Structure_and_Function_of_Vertebral_Trabecular.5.aspx

40. Swartz, E. E., Floyd, R. T., & Cendoma, M. (2005). Cervical spine functional anatomy and the biomechanics of injury due to compressive loading. *Journal of Athletic Training*, *40*(3), 155–161.

41. Tan, L. A., Riew, K. D., & Traynelis, V. C. (2017). Cervical Spine Deformity - Part 1: Biomechanics, Radiographic Parameters, and Classification. *Neurosurgery*, *81*(2), 197–203. https://doi.org/10.1093/neuros/nyx249

42. Thomas, W. B., & Fingeroth, J. M. (2015). Spondylosis Deformans. In *Advances in Intervertebral Disc Disease in Dogs and Cats*. Elsevier Inc. https://doi.org/10.1002/9781118940372.ch8

43. Urban, J. P. G., & Roberts, S. (2003). Degeneration of the intervertebral disc. *Arthritis Research and Therapy*, *5*(3), 120–130. https://doi.org/10.1186/ar629

44. van der Kraan, P. M., & van den Berg, W. B. (2007). Osteophytes: relevance and biology. *Osteoarthritis and Cartilage*, *15*(3), 237–244. https://doi.org/10.1016/j.joca.2006.11.006

45. Waxenbaum, J. A., & Futterman, B. (2018a). Anatomy, Back, Cervical Vertebrae. In *StatPearls*. StatPearls Publishing. http://www.ncbi.nlm.nih.gov/pubmed/29083805

46. Waxenbaum, J. A., & Futterman, B. (2018b). Anatomy, Back, Cervical Vertebrae. In *StatPearls*. StatPearls Publishing. http://www.ncbi.nlm.nih.gov/pubmed/29083805

47. Waxenbaum, J. A., & Futterman, B. (2019). Anatomy, Back, Lumbar Vertebrae. In

StatPearls. StatPearls Publishing. http://www.ncbi.nlm.nih.gov/pubmed/29083618

48. Weissman, B. N. (2009). Osteoarthritis. *Imaging of Arthritis and Metabolic Bone Disease*, 107–133. https://doi.org/10.1016/B978-0-323-04177-5.00008-2
49. *Welcome to RadiAnt DICOM Viewer*. (n.d.). Retrieved April 5, 2021, from https://www.radiantviewer.com/dicom-viewer-manual/index.html
50. Wu, J. Y., & Lee, R. (1997). The advantages of triangular and tetrahedral edge elements for electromagnetic modeling with the finite-element method. *IEEE Transactions on Antennas and Propagation*, *45*(9), 1431–1437. https://doi.org/10.1109/8.623133
51. Zhang, Q. H., Teo, E. C., Ng, H. W., & Lee, V. S. (2006). Finite element analysis of moment-rotation relationships for human cervical spine. *Journal of Biomechanics*, *39*(1), 189–193. https://doi.org/10.1016/j.jbiomech.2004.10.029
52. Zienkiewicz, O. C. (2013). The Finite Element Method: Its Basis and Fundamentals. *The Finite Element Method: Its Basis and Fundamentals*, iii. https://doi.org/10.1016/b978-1-85617-633-0.00020-4

Chapter VI: Annexes

Annex 1

Table 1: ICEM configuration for the mesh

Global Mesh Size	Global Element Scale Factor	Scale Factor	**1,3**
	Global Element Seed Factor	Max Element	**1**
	Curvature/Proximity Based Refinement	Min Size Limit	**0,5**
		Element Gap	**1**
		Refinement	**10**
Prism Meshin Parameters	Groth Law	**Exponential**	
	Initial Height	**0**	
	Height Ratio	**1,1**	
	Number of Layers	**5**	
	Total Height	**0,5**	
	Fix Maching Direction	**No**	
	Min Prism Quality	**0.0099999998**	
	Filler Ratio	**0.1**	
	Max Prism Angle	**180**	
	Max Heigth over Base		
	Prism Heigth Limit	**0**	
	Prism Element Part Controls	New Volume Part	**No**
		Side Part	**No**
		Top Part	**No**
	Smoothing Options	Number of surface smoothing steps	**5**
		Triangle quality type	**inscribed_area**
		Ortho weight	**0,5**
		Number of volume smoothing steps	**10**

		First layer smoothing steps	**1**
		Max Directional smoothing steps	**10**
	Additional Ple Inflation (Fluent Meshing) settings	Fix First Layer	**No**
		Number of Orthogonal Layers	**0**
		Gap Factor	**0,5**
		Enhance Normal Computation	**No**
		Enhance Offset Computation	**No**
		Smoothing Level	**Medium**
		Max Allowable Cap Skewness	**0.98**
		Max Allowable Cell Skewness	**0.90**
Volume Meshing Parameters	Mesh Type	**Tetra/Mixed**	
	Tetra/Mixed Meshing	Mesh Method	**Robust (Octree)**
		Run as batch process	**No**
		Fast transition	**No**
		Edge criterion	**0,2**
		Define thin cuts	**No**
		Smooth mesh	**Yes**
		Smooth Iterations	**0**
		Min quality	**0,4**
		Coarsen mesh	**No**

		Coarsen Iterations	**2**
		Worst 72specto ratio	**0,2**
		Fix Non-manifold	**Yes**
		Close Gaps	**No**
		Fix Holes	**Yes**
		Use active local coordinate system	**No**
Volume Mesh	Mesh Type	**Tetra/Mixed**	
Tetra/Mixed Mesh	Mesh Method	**Robust Octree**	
	Create Prism Layers	**No**	
	Create Hexa-Core	**No**	
	Select Geometry	**All**	
	Use Existing Mesh Parts	**No**	

Note: All the configuration that I used to generate the mesh.

Annex 2

Figure 1: Strain (E22)

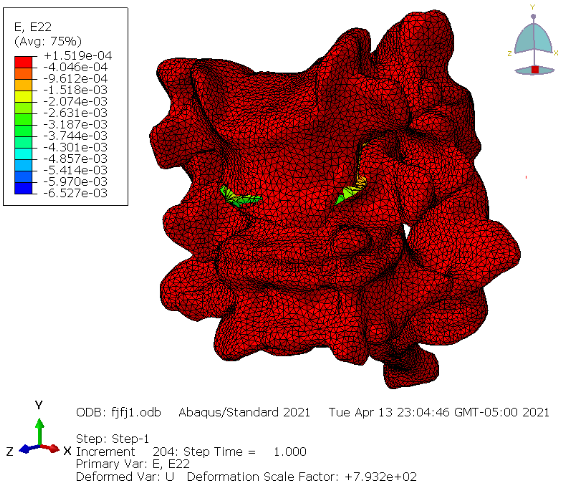

Figure 2: Stress (S11)

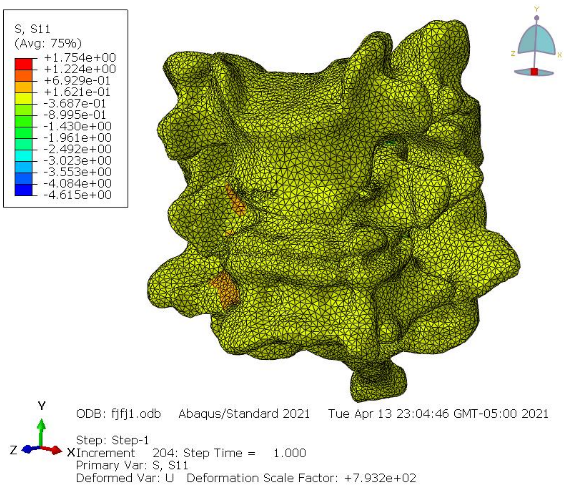

Table 2: Stress (S11) vs Strain (E22)

Data

Strain	Stress
1,95416E-06	4,91999E-06
3,91E-06	9,83998E-06
6,83956E-06	1,722E-05
1,12364E-05	2,82899E-05
0,000223018	0,000561494
0,000232789	0,000586094
0,00024256	0,000610694
0,000252331	0,000635294
0,000262102	0,000659894
0,000467288	0,001176492
0,000799495	0,002012891
0,000809266	0,002037491
0,000819037	0,00206209
0,001258723	0,003169088
0,001483451	0,003734887
0,001493222	0,003759487
0,001502992	0,003784087
0,001512763	0,003808687
0,001522534	0,003833287
0,001532305	0,003857887
0,001649554	0,004153086
0,001659325	0,004177686
0,001669096	0,004202286
0,001678867	0,004226886
0,001688638	0,004251486
0,001698408	0,004276086
0,001708179	0,004300686
0,00171795	0,004325286
0,001727721	0,004349886
0,001893824	0,004768085
0,001903595	0,004792685
0,001913366	0,004817285
0,001923137	0,004841885
0,001932907	0,004866485
0,001942678	0,004891085
0,001952449	0,004915684
0,001954159	0,00491999

Annex 3

Figure 3: X displacement

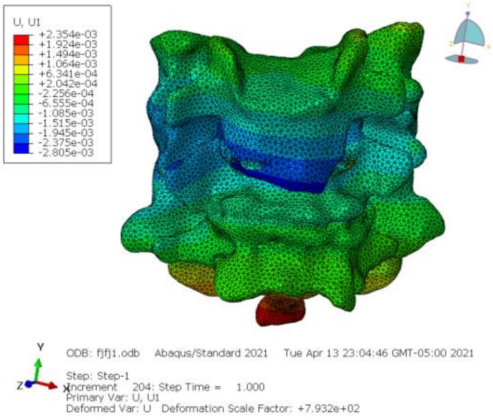

Table 3: Time vs X-axis displacement Data

Frame	U
0,001	2,5652E-06
0,002	5,1304E-06
0,0035	8,9782E-06
0,00575	1,475E-05
0,009125	2,3407E-05
0,014125	3,6233E-05
0,019125	4,9059E-05
0,024125	6,1885E-05
0,029125	7,4711E-05
0,069125	0,00017732
0,074125	0,00019014
0,079125	0,00020297
0,084125	0,0002158
0,089125	0,00022862
0,094125	0,00024145
0,099125	0,00025427
0,104125	0,0002671
0,109125	0,00027993
0,21412501	0,00054927
0,219125	0,0005621
0,224125	0,00057492
0,22912499	0,00058775
0,234125	0,00060057
0,239125	0,0006134
0,46412501	0,00119057
0,469125	0,00120339
0,474125	0,00121622
0,47912499	0,00122905
0,48412499	0,00124187
0,48912501	0,0012547
0,49412501	0,00126752
0,51912498	0,00133165
0,52412498	0,00134448
0,52912498	0,00135731
0,53412497	0,00137013
0,53912503	0,00138296
0,54412502	0,00139578
0,54912502	0,00140861
0,814125	0,00208838
0,86412501	0,00221664
0,86912501	0,00222947
0,874125	0,0022423
0,879125	0,00225512
0,88412499	0,00226795
0,88912499	0,00228077
0,89412498	0,0022936
0,89912498	0,00230642
0,90412498	0,00231925
0,90912497	0,00233208
0,91412503	0,0023449
0,91912502	0,00235773
0,92412502	0,00237055
0,92912501	0,00238338
0,93412501	0,00239621
0,939125	0,00240903
0,944125	0,00242186
0,94912499	0,00243468
0,95412499	0,00244751
0,95912498	0,00246034
0,96412498	0,00247316
0,96912497	0,00248599
0,97412503	0,00249881
0,97912502	0,00251164
0,98412502	0,00252447
0,98912501	0,00253729
0,99412501	0,00255012
0,999125	0,00256294
1	0,00256519

Annex 4

Figure 4: Y-axis displacement

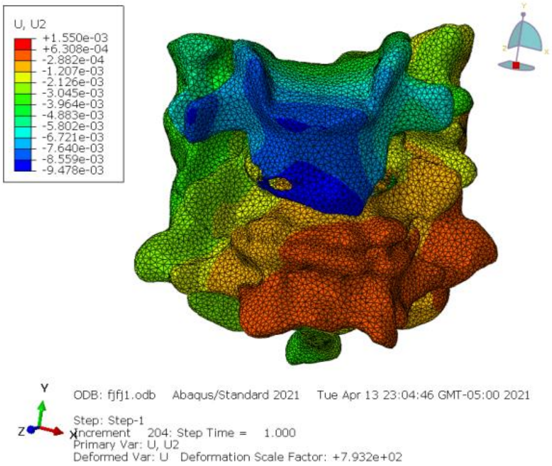

Table 4: Time vs Y-axis displacement Data

Frame	U
0,001	8,0337E-06
0,002	1,6067E-05
0,0035	2,8118E-05
0,00575	4,6194E-05
0,009125	7,3308E-05
0,014125	0,00011348
0,019125	0,00015365
0,024125	0,00019381
0,029125	0,00023398
0,044125	0,00035449
0,26912501	0,00216208
0,27412501	0,00220225
0,27912501	0,00224242
0,284125	0,00228259
0,289125	0,00232276
0,29412499	0,00236293
0,29912499	0,00240309
0,30412501	0,00244326
0,30912501	0,00248343
0,314125	0,0025236
0,319125	0,00256377
0,32412499	0,00260394
0,32912499	0,00264411
0,33412501	0,00268427
0,33912501	0,00272444
0,344125	0,00276461
0,349125	0,00280478
0,35412499	0,00284495
0,35912499	0,00288512
0,36412501	0,00292529
0,36912501	0,00296546
0,374125	0,00300562
0,379125	0,00304579
0,38412499	0,00308596
0,38912499	0,00312613
0,39412501	0,0031663
0,39912501	0,00320647
0,40412501	0,00324664
0,409125	0,00328681
0,414125	0,00332697
0,41912499	0,00336714
0,42412499	0,00340731
0,52912498	0,00425086
0,53412497	0,00429102
0,53912503	0,00433119
0,54412502	0,00437136
0,54912502	0,00441153
0,55412501	0,0044517
0,55912501	0,00449187
0,564125	0,00453204
0,73912501	0,00593794
0,74412501	0,00597811
0,749125	0,00601828
0,754125	0,00605845
0,75912499	0,00609862
0,76412499	0,00613878
0,76912498	0,00617895
0,95412499	0,0076652
0,95912498	0,00770536
0,96412498	0,00774553
0,96912497	0,0077857
0,97412503	0,00782587
0,97912502	0,00786604
0,98412502	0,00790621
0,98912501	0,00794638
0,99412501	0,00798655
0,999125	0,00802671
1	0,00803374

Annex 5

Figure 5: Z-axis displacement

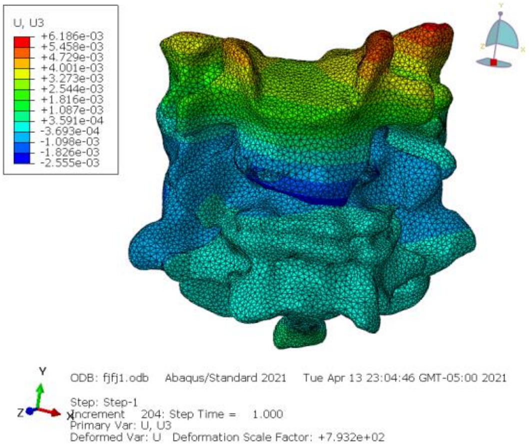

Table 5: Time vs Z-axis displacement Data

Frame	U
0,001	2,2035E-06
0,002	4,4071E-06
0,0035	7,7124E-06
0,00575	1,267E-05
0,009125	2,0107E-05
0,014125	3,1125E-05
0,019125	4,2143E-05
0,024125	5,316E-05
0,029125	6,4178E-05
0,099125	0,00021843
0,104125	0,00022944
0,109125	0,00024046
0,114125	0,00025148
0,119125	0,0002625
0,18412501	0,00040573
0,189125	0,00041674
0,194125	0,00042776
0,21412501	0,00047183
0,219125	0,00048285
0,224125	0,00049387
0,22912499	0,00050489
0,234125	0,0005159
0,239125	0,00052692
0,24412499	0,00053794
0,249125	0,00054896
0,254125	0,00055997
0,25912499	0,00057099
0,26412499	0,00058201
0,26912501	0,00059303
0,27412501	0,00060404
0,27912501	0,00061506
0,284125	0,00062608
0,289125	0,0006371
0,29412499	0,00064812
0,29912499	0,00065913
0,30412501	0,00067015
0,30912501	0,00068117
0,314125	0,00069219
0,319125	0,0007032
0,32412499	0,00071422
0,629125	0,0013863
0,63412499	0,00139732
0,63912499	0,00140834
0,64412498	0,00141935
0,64912498	0,00143037
0,65412498	0,00144139
0,754125	0,00166174
0,75912499	0,00167276
0,76412499	0,00168378
0,76912498	0,0016948
0,77412498	0,00170581
0,879125	0,00193719
0,88412499	0,0019482
0,88912499	0,00195922
0,89412498	0,00197024
0,89912498	0,00198126
0,90412498	0,00199227
0,90912497	0,00200329
0,92912501	0,00204736
0,93412501	0,00205838
0,939125	0,0020694
0,95412499	0,00210245
0,95912498	0,00211347
0,96412498	0,00212449
0,96912497	0,0021355
0,97412503	0,00214652
0,97912502	0,00215754
0,98412502	0,00216856
0,98912501	0,00217957
0,99412501	0,00219059

0,999125	0,00220161
1	0,00220354

Annex 6

Table 6: Time vs Pressure of an Integration Point Data

Frame	P
0,001	0,00943177
0,002	0,01886354
0,0035	0,03301119
0,00575	0,05423267
0,009125	0,0860649
0,014125	0,13322373
0,019125	0,18038259
0,024125	0,22754143
0,029125	0,27470028
0,034125	0,32185912
0,039125	0,36901796
0,044125	0,41617683
0,049125	0,46333563
0,054125	0,51049447
0,24412499	2,30253053
0,249125	2,34968948
0,254125	2,39684844
0,25912499	2,44400716
0,26412499	2,49116588
0,26912501	2,53832483
0,27412501	2,58548379
0,27912501	2,63264251
0,284125	2,67980123
0,289125	2,72696018
0,29412499	2,77411914
0,36912501	3,48150182
0,374125	3,52866077
0,379125	3,57581973
0,47912499	4,51899672
0,48412499	4,56615496
0,48912501	4,61331415
0,49412501	4,66047287
0,499125	4,70763206
0,54412502	5,13206148
0,54912502	5,17921972
0,55412501	5,22637939
0,55912501	5,27353811
0,564125	5,32069635
0,569125	5,36785555
0,57412499	5,41501427
0,57912499	5,46217346
0,58412498	5,50933218
0,58912498	5,55649137
0,59412497	5,60364962
0,59912503	5,65080833
0,60412502	5,69796753
0,60912502	5,74512672
0,61412501	5,79228544
0,61912501	5,83944368
0,77912498	7,34852743
0,78412497	7,39568567
0,78912503	7,44284487
0,79412502	7,49000359
0,79912502	7,53716278
0,80412501	7,5843215
0,80912501	7,63147974
0,814125	7,67863894
0,819125	7,72579813
0,82412499	7,77295685
0,82912499	7,82011557
0,83412498	7,86727476
0,83912498	7,91443396
0,84412497	7,9615922
0,84912503	8,00875092
0,85412502	8,05590916
0,85912502	8,10306835
0,874125	8,24454498
0,879125	8,29170418
0,88412499	8,33886242
0,88912499	8,38602161
0,89412498	8,43318081
0,89912498	8,48034
0,90412498	8,52749825
0,90912497	8,57465744
0,91412503	8,62181568
0,91912502	8,66897488
0,92412502	8,71613407
0,95912498	9,04624557
0,96912497	9,14056301

0,97412503	9,18772221
0,97912502	9,23488045
0,99412501	9,37635708
1	9,43176937